Simulations of a passively actuated oscillating airfoil using a Discontinuous Galerkin method

by

Emily Renee Israeli

Submitted to the Department of Aeronautics and Astronautics
in partial fulfillment of the requirements for the degree of

Master of Science in Aeronautics and Astronautics

at the

MASSACHUSETTS INSTITUTE OF TECHNOLOGY

August 2008

Author . . . .
Department of Aeronautics and Astronautics
August 21, 2008

Certified by . . . .
Prof. Jaime Peraire
Professor
Thesis Supervisor

Accepted by . . . .
Prof. David L. Darmofal
Associate Department Head
Chair, Committee on Graduate Students

Simulations of a passively actuated oscillating airfoil using a Discontinuous Galerkin method

by

Emily Renee Israeli

Submitted to the Department of Aeronautics and Astronautics
on August 21, 2008, in partial fulfillment of the
requirements for the degree of
Master of Science in Aeronautics and Astronautics

Abstract

Natural flappers, such as birds and bats, effectively maneuver in transitional, low Reynolds number flow, outperforming any current small engineered flapping vehicle. Thus, engineers are inspired to investigate the flapping dynamics present in nature to further understand the non-tradional flow aerodynamics in which they operate. Undeniably the success of biological flapping flight is the exploitation of fluid structure interaction response i.e. wing mechanics, deformation, and morphing. Even though all these features are encountered in nature, it is important to note that natural flappers have not just adapted to optimize their aerodynamic behavior, they also have evolved due to biological constraints. Therefore, in bio-inspired design one carefully uses the insight gained from understanding natural flappers.

Here, a 2-D simulation of a pitching and heaving foil attempts to indicate flapping parameter specifics that generate an efficient, thrust producing flapper. The simulations are performed using a high-order Discontinuous Galerkin finite element solver for the compressible Navier Stokes equations. A brief investigation of a simple problem in which pitch and heave of a foil are prescribed highlights the necessity to use an inexpensive lower fidelity model to narrow down the large design space to a manageable region of interest. A torsional spring is placed at the foil's leading edge to passively modulate the pitch while the foil is harmonically heaved. This model gives the foil passive structural compliance that automatically determines the pitch. The two-way fluid structure interaction thus results from the simultaneous resolution of the fluid and moment equations. This thesis explores the pitch profile and force generation characteristics of the spring-driven, oscillating foil. The passive strategy is found to enhance the propulsive efficiency and thrust production of the flappers specifically in cases where separation is encountered. Furthermore, the passive spring system performs like an ideal actuator that enables the oscillating foil to extract energy from the fluid motion without additional power input. Thus, this is the optimal mechanism to drive the foil dynamics for efficient flight with kinematic flexibility.

Thesis Supervisor: Prof. Jaime Peraire
Title: Professor

Acknowledgments

First and foremost I would like to express my gratitude to my research advisor, Prof. Jaime Peraire, for his guidance, support, and encouragement during the past two years. I want to thank Dave Willis for all the flapping flight discussions, assisting me in my research, guiding me through all the setbacks, and listening to all my ideas. I would not have been able to complete this thesis without your day-to-day input and dedication. I thank Prof. Per-Olof Persson for pioneering 3DG which is the code used for all the simulations in my thesis and all the debugging help. I have become a better programmer because of you.

I also want to thank my colleague, Alejandra Uranga. I am going to miss working with you. Our friendship means so much to me. You always managed to cheer me up and make me smile. I thank Britt Bille Rasmussen who always is willing to listen and help out with challenges. Also, thank you to all my colleagues in the Aerospace Computation Design Lab.

I would like to thank my family and friends for their unconditional love and support. I acknowledge the commitment of my Mom and Dad to me. I cannot repay them for their integral part in my scientific successes and endeavors. I also want to express my gratitude to my sister, Lisa Isaacs, and her family for their encouragement. Special thanks to both my brothers and their families. Lastly, I thank my friend, Rachel Schecter, who has supported me, encouraged me, and always is around when I need it.

Contents

List of Figures

List of Tables

Chapter 1

Introduction

With the development of Micro Aerial Vehicles (MAVs) and flapping wing vehicles, there has been growing interest in the complex fluid dynamics of transitional, low Reynolds number flow in an attempt to improve the design of these engineered systems. Commonly, this aerodynamic regime involves phenomena such as fluid structure interaction and unsteady flow effects in which the physics is still relatively unknown. Natural flappers such as birds and bats fly in this adverse flow environment, yet perform effectively. Observing the success of biological flapping flight, scientists and engineers are determined and inspired to further comprehend low Reynolds number flow to adapt the design of small engineered vehicles to realize more efficient flight. A high order Discontinuous Galerkin finite element discretization provides the potential to assess and fully resolve non-traditional flapping flight physics e.g. fluid structure interaction. The goal here is to further understand details of flapping flight by simulating a passively actuated oscillating airfoil and thus gain insight into bio-inspired vehicle design.

Chapter two describes the Navier Stokes equations for compressible flow as well as the methodology of the Discontinuous Galerkin method including formulation, discretization, and solver.

Chapter three presents the approach to solving the fluid-structure coupling characteristic of flapping flight and describes the spring structural model of the oscillating foil.

Chapter four displays simulation results that attempt to ascertain several phenomena of flapping flight, particularly trying to characterize optimal flapping motion and flapping parameters. Both prescribed and passively modulated pitching and heaving airfoil simulations are performed.

Chapter five concludes with a summary of the results and discusses the effectiveness of passive compliance in the flapping foil model.

1.1 Flapping flight

In nature, flappers successfully overcome unsteady low Reynolds number transitional flows. However, while effective flapping flight has been attaoned by bats and birds, engineered flapping vehicles such as Uninhabitated Micro Aerial Vehicles (UAVs and MAVs) still lack the capability to overcome the adverse flow conditions in which they operate. Thus, there is a blossoming in the examination of biological flapping flight that encompasses the variable transitional and low Reynolds number (Re=15,000-70,000) [13] aerodynamic regime. Furthermore, to gain headway in the less conventional human design of flapping wing vehicles (unlike conventional fixed wing-tube aircraft engineering), engineers and researchers attempt to further understand the flow physics and structural mechanics of natural flappers to eventually be able to mimic their ability. Nature outperforms human design by exploiting the large deformation fluid-structure coupling [27] as well as active and passive wing response (configuration and dynamics) [1],[29]. The limitation of MAV capability is at least partly due to inefficient power conversion of the flight system; however, energy storage to enable long range flight and lack of maneuverability (e.g. hovering) are the major obstacles hindering an effective design. The engineered flight vehicles need to incorporate the ability of bats and birds to realize effective flapping flight by exploiting passive compliance and active morphing despite unpredictable flight conditions.

Still the endless aerodynamic complexities of flapping flight remain largely ununderstood. Particularly, the natural flyers invoke a favorable response mechanism, changing their wing dynamics and shape. This response is modulated by fluid structure interaction and allows the flapper to maintain efficient flight. In nature, the compliant wing motion and active wing morphing is fine tuned for achieving efficient aerodynamics. However, the exploration of natural flappers is confined to the flight design space of the animal's operating conditions and biological constraints. Thus, the animals give insight into the requirements of flapping flight but their contribution to the design process is also limited.

In the last twenty years, biologists have begun to do hardcore research on the flight mechanics of insects, birds and recently bats in an attempt to reveal the mechanisms of these creatures flight dynamics. All natural flappers have a component of compliance in their wing dynamics that contributes to their flapping propulsive efficiency. Many computational investigations have been performed to study flapping flight and flapping propulsive efficiency [27], [28]. This thesis uniquely employs an inverse strategy where in the early stages of design, lower fidelity models give quick preliminary parameter space knowledge relating to effective flapping flight. Then, a high fidelity model of a refined design space looks to minimize both wake induced and viscous losses of the unsteady model. The design and analysis of the unsteady fluid structure interaction associated with flapping airfoils attempts to comprehend parameters such as flapping amplitude, frequency in terms of pitch and heave as well as the lag between pitch and heave.

1.2 Computational approach

The Discontinuous Galerkin (DG) finite element method is recently of growing interest as an approach to solve fluid problems. The high order method has the ability to generate extremely accurate solutions with minimal numerical dispersion. Real world applications involving fluid structure interaction require the computation of time-dependent solutions, in particular to Navier Stokes coupled to a structural model on a deformable domain [17]. Also, DG methods generate stable discretizations of the convective operator for any order discretization. To account for moving geometry, the Arbitrary Lagrangian-Eulerian (ALE) method is employed. The details of this paper's computational approach are in [19] as well as presented in section 3 of this thesis. There are currently many other approaches to fluid structure interaction simulations [6], [21], [32] as well as ALE on deformable domains [2], [5], [14], [26]. Due to the brief description of the development of DG, the reader is referred to the references or to the work describing the method in [17].

In order to obtain maximum geometrical flexibility the compressible Navier-Stokes equations are discretized on unstructured triangular meshes which is a requirement of real world geometries. Furthermore, the code accommodates for time changing geometry by implementing an ALE formulation on deformable meshes. The time integration for the fluid can be carried out either implicitly or explicitly, here we focus on the implicit formulation

1.3 Objective

The design of an efficient, thrust producing, harmonically driven pitching and heaving foil is considered. For this, the leading edge motion is prescribed using a sinusoidal function (heaving) that defines the foil's vertical position. The airfoil's pitching is actuated by a leading edge torsional spring; the airfoils propensity to conform to the fluid motion is then specified by a prescribed spring constant. The full two-way fluid structure interaction thus results from the simultaneous resolution of the fluid and moment equations. Moreover, the leading edge spring attempts to incorporate passive compliance to achieve efficient flapping.

Chapter 2

Methodology

2.1 Governing equations of fluid flow

We consider the compressible Navier-Stokes equation in conservative form [23]

$$\frac{\partial \rho}{\partial t} + \frac{\partial \left(\rho u_j\right)}{\partial x_j} = 0 \tag{2.1}$$

$$\frac{\partial \left(\rho u_i\right)}{\partial t} + \frac{\partial \left(\rho u_i u_j\right)}{\partial x_j} = -\frac{\partial p}{\partial x_i} + \frac{\partial \tau_{ji}}{\partial x_j} \tag{2.2}$$

$$\frac{\partial \left(\rho E\right)}{\partial t} + \frac{\partial \left[u_j \left(\rho E + p\right)\right]}{\partial x_j} = \frac{\partial \left(u_i \tau_{ji}\right)}{\partial x_j} - \frac{\partial q_j}{\partial x_j} \tag{2.3}$$

where shear stress and heat flux are given respectively by

$$\tau_{ij} = \mu \left(\frac{\partial u_i}{\partial x_j} + \frac{\partial u_j}{\partial x_i} - \frac{2}{3} \frac{\partial u_k}{\partial x_k} \delta_{ij} \right) \tag{2.4}$$

$$q_j = -\frac{\mu}{Pr} \frac{\partial}{\partial x_j} \left(E + \frac{p}{\rho} - \frac{1}{2} u_k u_k \right) \tag{2.5}$$

and where γ is the ratio of specific heats c_p/c_v, Pr is the molecular Prandtl number $\mu c_p/\kappa$, and μ is the molecular dynamic viscosity where constant viscosity is assumed and determined by setting the Reynolds number. Also ρ is the fluid density, u_i are the velocity components, p is the static pressure assuming ideal gas law

$$p = \rho \left(\gamma - 1\right) \left(E - \frac{1}{2} u_k u_k \right) , \tag{2.6}$$

E is the total energy, and H is the total enthalpy defined as $H = E + p/\rho$.

2.2 Discontinuous Galerkin method

2.2.1 Formulation

For the DG numerical solver, we rewrite the problem as system of first order equations [15]. Before generating this system, we consider the Navier-Stokes equations from section 2.1 as a time-dependent conservation law of the form

$$\frac{\partial U}{\partial t} + \nabla \cdot F_{\text{inv}}(U) - \nabla \cdot F_{\text{visc}}(U, \nabla U) = S(U, \nabla U) \tag{2.7}$$

in domain Ω with suitable boundary conditions and where F_{inv} denotes the inviscid fluxes and F_{visc} denotes the viscous fluxes. We are solving the compressible Navier-Stokes equations (2-D) where U is the state vector of variables

$$U = \begin{bmatrix} \rho \\ \rho u \\ \rho v \\ \rho E \end{bmatrix}.$$

The inviscid fluxes F_{inv} are given by

$$F_{\text{inv}}(U) = \begin{bmatrix} \rho u & \rho v \\ \rho u u + p & \rho u v \\ \rho v u & \rho v v + p \\ \rho u H & \rho v H \end{bmatrix},$$

and the viscous fluxes F_{visc} are given by

$$F_{\text{visc}}(U,\nabla U)=\begin{bmatrix}0 & 0\\ \tau_{xx} & \tau_{xy}\\ \tau_{xy} & \tau_{yy}\\ u\tau_{xx}+v\tau_{xy}+\frac{\gamma}{Pr}E_x & u\tau_{xy}+v\tau_{yy}+\frac{\gamma}{Pr}E_y\end{bmatrix}$$

where $\tau_{xx}=2u_x+\lambda(u_x+v_y)$, $\tau_{xy}=v_x+u_y$, $\tau_{yy}=2v_x+\lambda(u_x+v_y)$ and $\lambda=-2\mu/3$. In the case of the Navier-Stokes equations, the source term S is zero. The above definitions are determined by simplifying the governing equations from section 2.1 to 2-D. Finally, before discretizing the equations, we eliminate the second order spatial derivatives of U by introducing additional variables $Q=\nabla U$. Thus, the equation (2.7) is reformulated as a system of first order equations

$$\begin{aligned}\frac{\partial U}{\partial t}+\nabla\cdot F_{\text{inv}}(U)-\nabla\cdot F_{\text{visc}}(U,Q) &= S(U,Q)\\ Q-\nabla U &= 0\,. \end{aligned}\tag{2.8}$$

2.2.2 Discretization

The DG discretization [18] of the system of equations in (2.8) involves the triangulation $\mathcal{T}_h$ of the spatial domain Ω. In general, the weak formulation is obtained by multiplying by test functions $V\in\mathcal{V}$ and $R\in\Sigma$ and integrating by parts over the entire domain Ω. In the discrete case, the nonlinear conservation law is enforced locally over each element K. Also, the discrete analog considers functions denoted with the subscript h. Consequently, the DG finite element spaces $\mathcal{V}_h$ and Σ_h associated with all the elements K in the triangulation $\mathcal{T}_h$ are introduced. Both $\mathcal{V}_h$ and Σ_h are spaces of polynomial functions of order $p\geq 1$ on each element K. The discrete solution U_h

and Q_h for all elements $K \in \mathcal{T}_h$ is given by

$$\int_K \frac{\partial U_h}{\partial t} V_h \, dV - \int_K \left[F_{\text{inv}}(U_h) - F_{\text{visc}}(U_h, Q_h) \right] \cdot \nabla V_h \, dV = \\ \int_K S(U_h, Q_h) \, V_h \, dA - \int_{\partial K} \left[\hat{F}_{\text{inv}} - \hat{F}_{\text{visc}} \right] \cdot \boldsymbol{n} \, V_h \, dA \quad \forall V_h \in \mathcal{V}_h \tag{2.9}$$

$$\int_K Q_h \cdot R_h \, dV = - \int_K U_h \nabla \cdot R_h \, dV + \int_{\partial K} \hat{U} \, R_h \cdot \boldsymbol{n} \, dA \quad \forall R_h \in \Sigma_h \tag{2.10}$$

with numerical flux functions $\hat{F}_{\text{inv}}(U_h^+, U_h^-)$, $\hat{F}_{\text{visc}}(U_h^+, U_h^-, Q_h^+, Q_h^-)$, and $\hat{U}(U_h^+, U_h^-)$ that are approximations to the fluxes on the boundary of each element ∂K. These numerical fluxes are determined by the left and right states at the boundary. The normal component of the numerical fluxes is enforced to be continuous across element interfaces to ensure conservation. Thus, the DG formulation is complete with the definition of the numerical fluxes. The inviscid numerical flux is determined using Roe's scheme [22]. On the other hand, the numerical fluxes $\hat{F}_{\text{visc}}$ and $\hat{U}$ are chosen using the Compact Discontinuous Galerkin (CDG) method [16]. Also, the numerical flux function $\hat{U}$ is chosen to be only a function of the degrees of freedom U_h (not Q_h) at the elemental level; thus, it is possible to cast a resulting system of equations that only involves the vector of quantities [4],[16] . Both the explicit and implicit solution approaches are addressed in section 2.4.

In this thesis, it is necessary to account for the time variation of the solution domain. Consequently, the general DG formulation of this section is transformed using Arbitrary Lagrangian Eulerian (ALE). In short, the Navier-Stokes equations as a conservation law for the independent variables are solved on a reference domain to account for the physical, time-varying geometries. The ALE formulation is addressed in section 2.3.

2.3 Arbitrary Lagrangian Eulerian formulation

Simulations involving fluid structure interaction have time-varying geometries; thus, the DG method needs to account for the mesh motion. The code uses an ALE

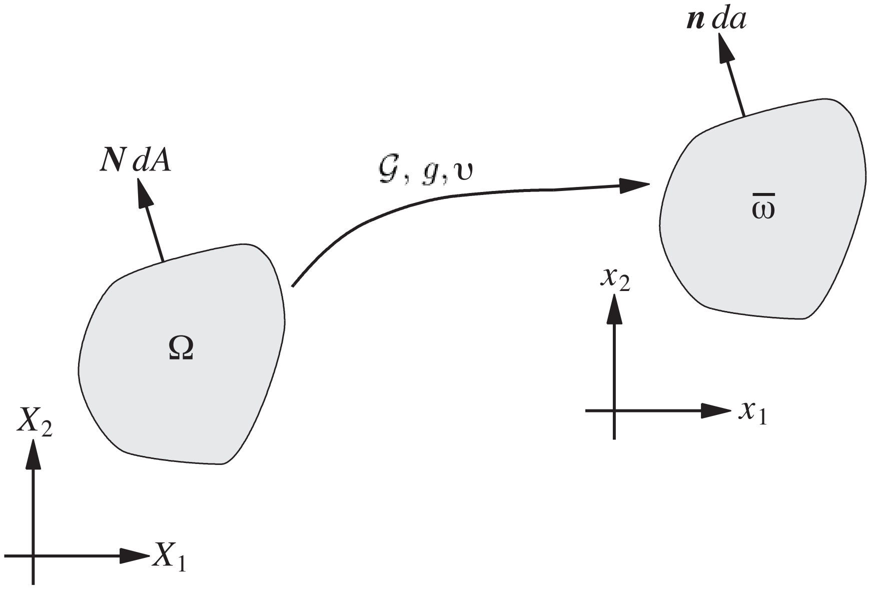

Figure 2-1: Reference domain Ω and physical domain $\bar{\omega}(t)$ configurations

formulation [19] which enables simulations on deformable domains while maintaining high order accuracy. The procedure involves a time dependent mapping between the physical domain and a fixed reference domain. With the mapping, the equations are transformed to obtain the physical solution.

2.3.1 Mapping

In order to effectively describe the mapping, a new notation is introduced. The time-dependent physical domain of the simulation is denoted $\bar{\omega}(t)$ and the corresponding fixed reference space is referred to as Ω. The one-to-one time dependent mapping between $\bar{\omega}(t)$ and Ω is $\mathcal{G}(X,t)$ where $x = \mathcal{G}(X,t)$ or in words $\mathcal{G}(X,t)$ maps a point X in Ω to a point $x(t)$ in $\bar{\omega}(t)$ (figure 2-1). With this mapping, the Navier-Stokes equations are continually solved on the reference domain in which the physical solution is determined by a transformation using the differential properties of the mapping. In addition, there are mappings for spatial and time derivatives necessary to transform the original Navier-Stokes equations on the physical domain to an equivalent conservation law on the reference domain (i.e. transform equations from $x(t)$ to X).

Mapping deformation gradient G and mapping velocity ν are

$$G = \nabla_X \mathcal{G}, \quad \nu = \left.\frac{\partial \mathcal{G}}{\partial t}\right|_X , \tag{2.11}$$

and the Jacobian of the mapping is defined as $g = \det(G)$.

Also important is the area change associated with the transformation between configurations. First, we define the small changes in length and elemental volumes relations (between reference and deformed domains) as $d\boldsymbol{x} = Gd\boldsymbol{X}$ and $dv = gdV$, respectively. Now, let the reference area be $d\boldsymbol{A} = \boldsymbol{N}\,dA$ and corresponding deformed area be $d\boldsymbol{a} = \boldsymbol{n}\,da$ where $\boldsymbol{N} \in \partial\Omega$ and $\boldsymbol{n} \in \partial\bar{\omega}(t)$ are unit vectors. Using the definition of an incremental change in volume $dV = d\boldsymbol{X} \cdot d\boldsymbol{A}$ in Ω and $dv = d\boldsymbol{x} \cdot d\boldsymbol{a}$ in $\bar{\omega}(t)$, we have the area change transformation from reference to deformable domain

$$\boldsymbol{n}\,da = gG^{-T}\boldsymbol{N}\,dA \tag{2.12}$$

and deformable to reference domain

$$\boldsymbol{N}\,dA = g^{-1}G^{T}\boldsymbol{n}\,da\,. \tag{2.13}$$

2.3.2 Transformed equations

The conservative form of Navier-Stokes equations in the physical domain (x, t) as seen in equation (2.7) is rewritten with subscripts x to signify the physical domain

$$\left.\frac{\partial U_x}{\partial t}\right|_x + \nabla_x \cdot F_x(U_x, \nabla U_x) = 0 \tag{2.14}$$

where $S_x(U_x, \nabla U_x) = 0$ and the flux term F_x is shorthand for both the inviscid and viscous fluxes, $F_x = F_{\text{inv}}(U_x) - F_{\text{visc}}(U_x, \nabla U_x)$. The consistent conservation law in the reference space is determined by manipulating the integral form of equation (2.14)

$$\int_{\bar{\omega}(t)} \left.\frac{\partial U_x}{\partial t}\right|_x dv + \int_{\partial\bar{\omega}} F_x \cdot \boldsymbol{n}\,da = 0\,, \tag{2.15}$$

in which the divergence theorem is applied to the second term (obtaining the area integral). In the integral form, the equation is transformed to the reference domain. The first term in the above expression becomes

$$\begin{aligned}\int_{\bar{\omega}(t)} \left.\frac{\partial U_x}{\partial t}\right|_x dv &= \frac{d}{dt}\int_{\bar{\omega}(t)} U_x dv - \int_{\partial\bar{\omega}} (U_x\nu)\cdot \boldsymbol{n}\, da \\ &= \frac{d}{dt}\int_{\Omega} g^{-1}U_x dV - \int_{\partial\Omega} (U_x\nu)\cdot (gG^{-T}\boldsymbol{N}) dA \\ &= \int_{\Omega} \left.\frac{\partial\left(g^{-1}U_x\right)}{\partial t}\right|_X dV - \int_{\partial\Omega} (gU_xG^{-1}\nu)\cdot \boldsymbol{N}\, dA\end{aligned} \tag{2.16}$$

via the Reynolds transport theorem, the volume transformation $dv = g\, dV$ and area change relation in equation (2.12). Now, the second term simply follows from the area transformation in equation (2.12)

$$\int_{\partial\gamma} F_x \cdot \boldsymbol{n}\, da = \int_{\partial\Gamma} F_x\cdot (gG^{-T}\boldsymbol{N}) dA = \int_{\partial\Gamma} (gG^{-1}F_x)\cdot \boldsymbol{N}\, dA\,. \tag{2.17}$$

Finally, with another application of the divergence theorem, the equivalent conservation for the reference configuration is

$$\left.\frac{\partial U_X}{\partial t}\right|_X + \nabla_X \cdot F_X(U_X, \nabla_X U_X) = 0\,, \tag{2.18}$$

where the tranformed state vector and fluxes in the reference domain are

$$U_X = gU_x\,, \quad F_X = gG^{-1}\left(F_x - U_x\nu\right) \tag{2.19}$$

and $\nabla_x U_x$ is derived by applying the chain rule.

When discretizing these transformed equations in the fixed reference domain, the Geometric Conservation Law (GCL) [19] needs to be satisfied in order to preserve the constant flow solution in the physical domain. For arbitrary mappings, the discrepancy results from small numerical errors in the Jacobian g during the time integration due to the transformation. To ensure preservation of the GCL, an additional equation for the determinant of the mapping g is solved simultaneously. Consequently, this correction allows a constant solution to be preserved [19], .

2.3.3 Rigid motion mapping

In general, rigid body motion in 2-D is described by both translation and rotation with mapping expression

$$x = r(t) + G_{\text{rigid}}(X - X_o)$$

where rotational mapping deformation gradient G_{rigid} is given by

$$G_{\text{rigid}} = \nabla_X x = \begin{bmatrix} \frac{\partial x}{\partial X} & \frac{\partial x}{\partial Y} \\ \frac{\partial y}{\partial X} & \frac{\partial y}{\partial Y} \end{bmatrix} = \begin{bmatrix} \cos\theta & \sin\theta \\ -\sin\theta & \cos\theta \end{bmatrix}$$

where $\theta(t)$ is the angle of rotation (pitch angle of the body with respect to X_o). The velocity of the mesh is given by

$$\nu = \dot{r} + \dot{G}_{\text{rigid}}(X - X_o)$$

where

$$\dot{G}_{\text{rigid}} = \nabla_X \nu = \begin{bmatrix} \frac{\partial \dot{x}}{\partial X} & \frac{\partial \dot{x}}{\partial Y} \\ \frac{\partial \dot{y}}{\partial X} & \frac{\partial \dot{y}}{\partial Y} \end{bmatrix} = \begin{bmatrix} -\dot{\theta}\sin\theta & \dot{\theta}\cos\theta \\ -\dot{\theta}\cos\theta & -\dot{\theta}\sin\theta \end{bmatrix}.$$

2.4 Solvers

The numerical scheme results in a system of ordinary differential equations (ODEs) of the form

$$M\frac{dU}{dt} = -R(U) \tag{2.20}$$

where M denotes the mass matrix, U is the global vector of the degrees of freedom associated with U_h, and $R(U)$ is the residual vector which is a nonlinear function of U. As in a regular finite element method nodal basis functions [10] are used to represent U_h in each element. With the initial condition $U(0) = U_0$, the system of ODEs generated from the numerical method are solved either explicitly using a fourth-order Runga-Kutta scheme or implicitly employing backward differentiation formula (BDF).

2.4.1 Explicit

For many of the unsteady simulations, time integration is implemented explicitly using a fourth-order Runga-Kutta scheme. The scheme is

$$\begin{aligned} U_{n+1} &= U_n + \frac{a_1}{6} + \frac{a_2}{3} + \frac{a_3}{3} + \frac{a_4}{6} + O(\Delta t^5) \\ a_1 &= \Delta t f(U_n, t_n) \\ a_2 &= \Delta t f\left(U_n + \frac{a_1}{2}, t_n + \frac{\Delta t}{2}\right) \\ a_3 &= \Delta t f\left(U_n + \frac{a_2}{2}, t_n + \frac{\Delta t}{2}\right) \\ a_4 &= \Delta f(U_n + a_3, t_n + \Delta t) \end{aligned} \tag{2.21}$$

where U_n refers to the solution at time $t_n = n\Delta t$ and $f(U_n, t_n) = -M^{-1}R(U_n)$.

For fluid structure applications, the flow and structure are coupled by integrating the equation corresponding to the additional structural variables simultaneously with the fluid system. The explicit approach entails timestep size restrictions, requiring very small timesteps to solve the desired unsteady simulations.

2.4.2 Implicit

The implicit backward differentiation formula of order k (BDF-k) [18]. is a method that approximates the time derivative of the solution as

$$\frac{\partial U}{\partial t} \simeq \frac{1}{\Delta t} \sum_{i=0}^{k} \alpha_i U_{n-i} \tag{2.22}$$

using solutions from k previous timesteps. In order to compute the new solution U_n at the next timestep n, the system becomes

$$M \sum_{i=0}^{k} \alpha_i U_{n-i} - \beta_k \Delta t R(U_n) = 0 \tag{2.23}$$

where α_i and β_k are coefficients that depend on the order of the solver (see appendix A for exact values of coefficients α_i and β_k for BDF-k, $k = 1, 2, 3$). We use Newton's method to solve. The initial guess of the Newton iteration, $U_n^{(0)}$ is the extrapolation from k previous solutions. The Newton iterates are updated by evaluating the linearized equation

$$J(U_n^{(j)}) \Delta U_n^{(j)} = R_{\mathrm{BDF}}(U_n^{(j)})\,, \tag{2.24}$$

until the BDF nonlinear residual is lower than a prescribed tolerance where j is the Newton iteration subscript. The BDF residual is defined as

$$R_{\mathrm{BDF}}(U_n) = M \sum_{i=0}^{k} \alpha_i U_{n-i} - \beta_k \Delta t R(U_n) \tag{2.25}$$

and the Jacobian J is the derivative of the BDF residual with respect to the degrees of freedom

$$J(U_n) = \frac{dR_{\mathrm{BDF}}}{dU_n} = \alpha_0 M - \beta_k \Delta t \frac{dR}{dU_n} \equiv M - \beta_k \Delta t K\,. \tag{2.26}$$

where $\alpha_0 = 1$ for all orders of BDF. The new iterates are $U_n^{(j+1)} = U_n^{(j)} - \Delta U_n^{(j)}$.

Chapter 3

Fluid structure coupling

We develop an implicit method for fluid structure coupling. By solving implicitly, the time integration is no longer restricted by mesh size. Thus, we are able to run unsteady simulations on fine meshes increasing the timestep by 3 orders of magnitude from explicit runs, still retaining high order accuracy.

3.1 Coupled system

The flow and structural system are solved simultaneously and coupled by appending the structural degrees of freedom to the state vector while performing the time integration. Thus, the state vector U from section 2.4 is

$$U = \begin{bmatrix} U_f \\ U_s \end{bmatrix} \tag{3.1}$$

where U_f and U_s are the fluid and structural states, respectively. For simple structural models i.e. rigid motion, the mesh motion is reduced to several structural parameters with an explicit mapping deformation gradient $G(U_s(t))$ (which describes rotation and translation in the case of rigid motion).

3.2 Implicit solver implementation

For the fluid states and additional structure equations, the BDF-k residual is the same as described in equation (2.25). In the case of the pitching and heaving foil, there is a very simple structural model based on a spring which results in two structural states: the pitch angle, θ, and its time derivative, $\dot{\theta}$, giving $U_s = [\theta, \dot{\theta}]$ (see section 3.2.2).

The Jacobian is identical to J defined in equation (2.26) but U now represents the coupled system. The residual derivative matrix K from equation (2.26) has the following matrix structure

$$K = \begin{bmatrix} & \uparrow \\ A & B \\ & \downarrow \\ \longleftarrow \quad C \quad \longrightarrow & D \end{bmatrix} = \begin{bmatrix} & \uparrow \\ \frac{\partial R_f}{\partial U_f} & \frac{\partial R_f}{\partial U_s} \\ & \downarrow \\ \longleftarrow \quad \frac{\partial R_s}{\partial U_f} \quad \longrightarrow & \frac{\partial R_s}{\partial U_s} \end{bmatrix} = \begin{bmatrix} & \uparrow \\ K_f & \frac{\partial R_f}{\partial \xi}\frac{d\xi}{dU_s} \\ & \downarrow \\ \longleftarrow \quad \frac{\partial R_s}{\partial \lambda}\frac{\partial \lambda}{\partial U_f} \quad \longrightarrow & K_s \end{bmatrix}$$

where λ is the flux quantity related to a fluid property (e.g.. force or moment) driving the structural motion, and $\xi = [x, y, \dot{x}, \dot{y}]$. The four inner matrices of the sensitivity matrix K have specific roles in the coupled system:

- $A = K_f$. The A matrix is just K_f (only related to the fluid system).

- $B = \frac{\partial R_f}{\partial \xi}\frac{d\xi}{dU_s}$. The B matrix relates the fluid fluxes to the structural degrees of freedom and is computed by simple chain rule. We compute the derivative of the fluid residual with respect to the mesh movement explicitly in the code. The mesh coordinates are directly related to the structural degrees of freedom through the mapping since $x = G(s)X$. Thus, the $d\xi/ds$ term is explicitly formed.

- $C = \frac{\partial R_s}{\partial \lambda}\frac{\partial \lambda}{\partial U_f}$. The C matrix links the flow variables interaction with the governing structural equations. The structural motion is generated by a flux quantity (for example, force on the body of the fluid) denoted λ giving $\partial R_s/\partial \lambda$. The flux-derived variable λ is related to the flow degrees of freedom by the chain rule where

$$\frac{\partial \lambda}{\partial U_f} = \frac{\partial F_X}{\partial U_f}\frac{\partial \lambda}{\partial F_X}, \qquad \frac{\partial F_X}{\partial U_f} = \frac{\partial F_x}{\partial U_f} - G^{-1}\nu \tag{3.2}$$

and F_X are the fluxes in the reference domain.

- $D = \frac{\partial R_s}{\partial U_s}$. The D matrix is the Jacobian of the structural system K_s.

Finally, the coupled system is solved directly using a sparse LU decomposition algorithm

$$\Delta U = -J^{-1} R_{\text{BDF}} \, . \tag{3.3}$$

Hence, this method is the general fluid structure interaction application developed. The next section details the B matrix for rigid body motion. Then, the specifics for a spring structural model is introduced.

3.2.1 Rigid motion case

For rigid motion with rotation θ and translation $r = (r_x, h)$ the transformation for the Jacobian B matrix can be written explicitly

$$\frac{d\xi}{dU_s} = \begin{bmatrix} \frac{dx}{d\theta} & \frac{dx}{d\dot\theta} & \frac{dx}{dr} & \frac{dx}{d\dot r} \\ \frac{dy}{d\theta} & \frac{dy}{d\dot\theta} & \frac{dy}{dr} & \frac{dy}{d\dot r} \\ \frac{d\dot x}{d\theta} & \frac{d\dot x}{d\dot\theta} & \frac{d\dot x}{dr} & \frac{d\dot x}{d\dot r} \\ \frac{d\dot y}{d\theta} & \frac{d\dot y}{d\dot\theta} & \frac{d\dot y}{dr} & \frac{d\dot y}{d\dot r} \end{bmatrix} = \begin{bmatrix} G_\theta \boldsymbol{X} & \mathbf{0} & \boldsymbol{I} & \mathbf{0} \\ -\dot\theta G \boldsymbol{X} & \frac{\dot G}{\dot\theta}\boldsymbol{X} & \mathbf{0} & \boldsymbol{I} \end{bmatrix} \tag{3.4}$$

where the point of rotation is set to $X_o = (0, 0)$ (thus, not in the equation above), $\xi = [x, y, \dot x, \dot y]$ is the vector of mesh positions and velocities, $U_s = [\theta, \dot\theta, r, \dot r]$ is the vector of structural degrees of freedom, G is the G_{rigid} defined in section 2.3.3 and G_θ is

$$G_\theta = \begin{bmatrix} -\sin\theta & \cos\theta \\ -\cos\theta & -\sin\theta \end{bmatrix} \tag{3.5}$$

(Also, note that $G_\theta = \frac{\dot{G}}{\dot{\theta}}$).

3.2.2 Spring structural model

The spring model is simpler than general rigid body motion in which only the rotation of the fluid described by the body's pitch angle θ interacts with the flow. Thus, the structural degrees of freedoms are just $U_s = [\theta, \dot{\theta}]$. The translation of the leading edge of the airfoil is prescribed using sinusoidal motion, $r = (0, h_o \cos(\omega t))$, a vertical motion set by a reduced frequency and amplitude, yielding a specific Strouhal number. The spring constant is given a natural frequency that determines the spring constant $C = I\omega_o^2$ which alters the airfoils propensity to conform to the fluid motion. The moment equation is solved simultaneously with the flow equations in order to capture the fluid-structure (spring) interaction. The particular moment equation being solved at the leading edge of the airfoil is

$$I\ddot{\theta} + C\theta - S\ddot{h} + M_f = 0 \tag{3.6}$$

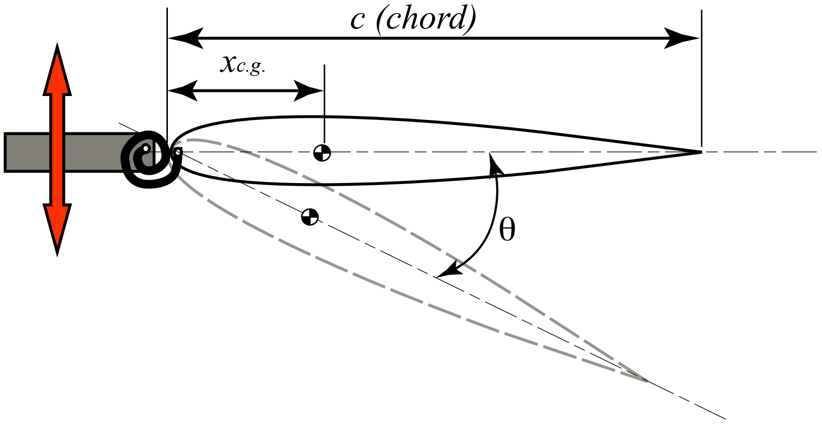

Figure 3-1: An illustration of the airfoil geometry used in this investigation. The unknown spring coefficient C is determined along with flapping parameters (such as flapping amplitude and flapping frequency) such that the thrust production is performed with high efficiency.

where I is the moment of inertia about the leading edge of the airfoil, C is the spring constant ($C = I\omega_o^2$, not to be confused with the C matrix of the residual derivative matrix K), $S = m_{\text{airfoil}}x_{cg}$ is the static unbalance or mass moment about the pivot and M_f is the moment generated by the fluid. As aforementioned, in this model the foil is pitching and heaving such that the heaving is described by $h = h_o \cos(\omega t)$ and θ is the foil's pitch angle actuated by the torsional spring.

For the implicit implementation, the spring equations are simply appended to the BDF-k residual as follows

$$R_{\text{BDF}} = \begin{bmatrix} M(U_n - \sum_{i=1}^{k} \alpha_i U_{n-i}) - \beta_k \Delta t R_f(U_n) \\ \theta_n - \sum_{i=1}^{k} \alpha_i \theta_{n-i} - \beta_k \Delta t \dot{\theta}_n \\ \dot{\theta}_n - \sum_{i=1}^{k} \alpha_i \dot{\theta}_{n-i} - \beta_k \Delta t \ddot{\theta}_n \end{bmatrix} \tag{3.7}$$

where the structural residuals ODEs for θ and $\dot{\theta}$,

$$R_s(\theta) = R_\theta = \frac{\partial \theta}{\partial t} = \dot{\theta}\,, \quad R_s(\dot{\theta}) = R_{\dot{\theta}} = \frac{\partial \dot{\theta}}{\partial t} = \ddot{\theta} \tag{3.8}$$

and

$$\ddot{\theta} = -\omega_o^2 \theta + \frac{S\ddot{h} - M_f}{I} \tag{3.9}$$

which is simply the moment equation (3.6) rearranged.

The Jacobian (derivative of the residual R) for the coupled fluid-spring system is

$$K = \left[\begin{array}{cc} & \uparrow \\ A & B \\ & \downarrow \\ \longleftarrow \; C \; \longrightarrow & D \end{array}\right] = \left[\begin{array}{ccc} & \uparrow & \uparrow \\ \frac{\partial R_f}{\partial U_f} & \frac{\partial R_f}{\partial \xi}\frac{d\xi}{d\theta} & \frac{\partial R_f}{\partial \xi}\frac{d\xi}{d\dot{\theta}} \\ & \downarrow & \downarrow \\ \longleftarrow \; \frac{\partial R_\theta}{\partial M_f}\frac{\partial M_f}{\partial U_f} \; \longrightarrow & \frac{\partial R_\theta}{\partial \theta} & \frac{\partial R_\theta}{\partial \dot{\theta}} \\ \longleftarrow \; \frac{\partial R_{\dot{\theta}}}{\partial M_f}\frac{\partial M_f}{\partial U_f} \; \longrightarrow & \frac{\partial R_{\dot{\theta}}}{\partial \theta} & \frac{\partial R_{\dot{\theta}}}{\partial \dot{\theta}} \end{array}\right] \tag{3.10}$$

where there are only two structural degrees of freedom $s = [\theta, \dot{\theta}]$ and $M_f = M_f(U, \theta, \dot{\theta})$

of equation (3.6). The inner matrices are derived such that

$$B = \begin{bmatrix} \uparrow & \uparrow \\ \frac{\partial R_f}{\partial \xi}\frac{d\xi}{d\theta} & \frac{\partial R_f}{\partial \xi}\frac{d\xi}{d\dot{\theta}} \\ \downarrow & \downarrow \end{bmatrix} = \frac{\partial R_f}{\partial \xi}\begin{bmatrix} G_\theta X & \mathbf{0} \\ -\dot{\theta} G X & \frac{\dot{G}}{\dot{\theta}} X \end{bmatrix} \tag{3.11}$$

accounting for the rigid body rotation about the leading edge of the body. and the C matrix is

$$C = \begin{bmatrix} \longleftarrow & \frac{\partial R_\theta}{\partial M_f}\frac{\partial M_f}{\partial U_f} & \longrightarrow \\ \longleftarrow & \frac{\partial R_{\dot{\theta}}}{\partial M_f}\frac{\partial M_f}{\partial U_f} & \longrightarrow \end{bmatrix} = \begin{bmatrix} \longleftarrow & 0 & \longrightarrow \\ \longleftarrow & -\frac{1}{I}\frac{\partial M_f}{\partial U_f} & \longrightarrow \end{bmatrix}. \tag{3.12}$$

Given the physical coordinates $x = GX$, the moment is the cross product between the position and the force over the boundary of the body $F_b = [f_X, f_Y]$ which are simply the integral of the boundary fluxes related to x- and y-moment equations

$$M_f = GX \times F_b = x f_Y - y f_X \tag{3.13}$$

$$\frac{\partial M_f}{\partial U_f} = \frac{\partial F_b}{\partial U_f}\frac{\partial M_f}{\partial F_b} = \frac{\partial f_Y}{\partial U_f}x - \frac{\partial f_X}{\partial U_f}y \tag{3.14}$$

where the sensitivities follow from the chain rule. Finally, we have

$$D = \frac{\partial R_s}{\partial s} = \begin{bmatrix} \frac{\partial R_\theta}{\partial \theta} & \frac{\partial R_\theta}{\partial \dot{\theta}} \\ \frac{\partial R_{\dot{\theta}}}{\partial \theta} & \frac{\partial R_{\dot{\theta}}}{\partial \dot{\theta}} \end{bmatrix} = \begin{bmatrix} 1 & 0 \\ \omega_o^2 + \frac{1}{I}\frac{\partial M}{\partial \theta} & \frac{1}{I}\frac{\partial M}{\partial \dot{\theta}} \end{bmatrix} \tag{3.15}$$

where the moment is dependent on the rotation of the body through terms

$$\frac{\partial M_f}{\partial \theta} = \frac{\partial M_f}{\partial \xi}\frac{d\xi}{d\theta}, \qquad \frac{\partial M_f}{\partial \dot{\theta}} = \frac{\partial M_f}{\partial \xi}\frac{d\xi}{d\dot{\theta}} \tag{3.16}$$

given by the chain rule shown in the expression above.

Chapter 4

Oscillating foil results

All simulations involve an oscillating HT13 airfoil with chord, $c = 1$, utilize the mesh in figure 4-1 and were conducted using a fourth order ($p = 4$) spatial discretization and a 2nd order BDF time integration scheme. Also, the fluid properties in the computations are $Re = 5 \times 10^3$, $Ma = 0.2$, and density $\rho = 1$.

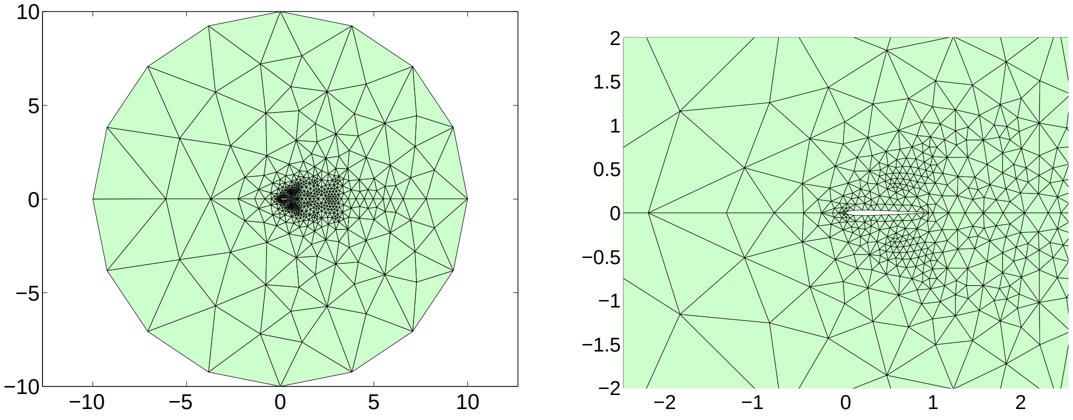

(a) mesh, 1054 elements

(b) zoom in on HT13 airfoil

Figure 4-1: Symmetric mesh for a HT13 airfoil, 1054 elements. All simulations were conducted using a fourth order ($p = 4$) spatial discretization and a 2nd order BDF time integration scheme.

4.1 Principal quantities of a flapping foil

Consider an airfoil as shown in figure 3-1 with chord length c and freestream velocity U. The oscillating airfoil is pitching and heaving prescribed by harmonic functions $\theta(t)$ and $h(t)$, respectively. The vertical plunge and angular motion have frequency ω with a phase lag ϕ between the harmonics. Let the heaving amplitude be h_o and pitching amplitude be θ_o. The pitching is assumed to be about the leading edge of the airfoil.

The airfoil's flapping dynamics are expressed by several characteristic non-dimensional numbers. The heave has a corresponding non-dimensional frequency, the Strouhal number,

$$St = \frac{\omega h_o}{U\pi}\,. \tag{4.1}$$

Also a reduced frequency, k, is defined by

$$k = \frac{\omega c}{2U} = \frac{\omega}{2} \tag{4.2}$$

where both U and c are unity.

Several relevant quantities convey the performance and energetics of the oscillating airfoils under the prescribed conditions described above. The unsteady force generation of the airfoil is quantified by drag $D(t)$, the horizontal (forward) force, and the lift $L(t)$, the vertical force (both in the frame of reference of the fluid not airfoil). We define time-varying force coefficients C_d and C_l given by

$$C_d(t) = \frac{D(t)}{\frac{1}{2}\rho U^2 c} = 2D(t) \quad , \quad C_l(t) = \frac{L(t)}{\frac{1}{2}\rho U^2 c} = 2L(t)\,. \tag{4.3}$$

The foil is also subject to a moment (torque) $M_f(t)$. Over a period of oscillation T, the time-averaged drag and lift forces are given by

$$\bar{D} = \frac{1}{T}\int_0^T D(t)\,dt\;,, \qquad \bar{L} = \frac{1}{T}\int_0^T L(t)\,dt\,. \tag{4.4}$$

respectively. The average thrust, $\bar{T}$ is equal in magnitude but opposite in direction to average drag and is non-dimensionalized to provide the thrust coefficient

$$C_t = -\frac{\bar{D}}{\frac{1}{2}\rho U^2 c} = \frac{\bar{T}}{\frac{1}{2}\rho U^2 c} \tag{4.5}$$

where a negative coefficient of thrust (positive drag) indicates an inefficient, drag producing flapper. The average power input per cycle ideally is the combined effect of the heaving and torquing actuation [3],

$$P_{\text{in}} = \frac{1}{T}\left(\int_0^T L(t)\dot{h}(t)\,dt + \int_0^T M_f(t)\dot{\theta}(t)\,dt\right)\,, \tag{4.6}$$

where $\dot{h}$ and $\dot{\theta}$ are given by analytical expressions (derivatives of prescribed sinusoids). The average power out corresponds to thrust generation as follows

$$P_{\text{out}} = \frac{1}{T}\int_0^T X_t(t)U\,dt\,. \tag{4.7}$$

Furthermore, the propulsive efficiency is defined to be the ratio of extracted power over input power

$$\eta = \frac{P_{\text{out}}}{P_{\text{in}}}\,. \tag{4.8}$$

Consider the same oscillating airfoil with harmonic vertical motion and a spring modulated pitch. The spring is a closed passive system, thus the torquing is no longer a component of the input power. On the other hand, the harmonic pitching airfoil with fully prescribed motion is actively rotating the foil (like a motor torque), thus included in the power in quantity. Moreover, for the passive spring oscillating foils the power input is just

$$P_{\text{in, spring}} = \frac{1}{T}\int_0^T L(t)\dot{h}(t)\,dt\,. \tag{4.9}$$

omitting the moment component from equation (4.6).

Analyzing the computational data involves integrating forces computed over various periods after the flow force/power generation stabilizes from incipient transient; however, for the cases where stall occurs the thrust generation continues to be somewhat unstabilized regardless of simulation time.

4.2 Prescribed actuation of foil motion

It is reasonable to think that one can prescribe the motion of an airfoil to be an efficient, thrust producing flapper; however, this strategy has a cumbersome parametric search. For example, only looking at the 2-D case of an oscillating airfoil both the pitch and the heave motion could be a sinusoid, triangular wave, square wave, and many other periodic motions, also to consider is the period of motion, the amplitude of pitch/heave, and the lag between pitch and heave. From aerodynamic intuition and the example of natural flappers, the design space can be narrowed. From low fidelity simulations, the ideal phase lag between pitch and heave is determined to be approximately 90° [31]. Also, one would expect the periodic motion to be relatively smooth without sudden changes in angle.

Thus, as an initial flapper design both a sinusoidal function for pitch and heave are prescribed at a 90° lag at reduced frequency of $k = 0.4$. The heave and pitch are described by $h(t) = h_o \cos \omega t$ and $\theta(t) = \theta_o \sin \omega t$, respectively, where $h_o/c = h_o$ and giving a corresponding Strouhal number. Non-dimensional parameters (aforementioned) are defined in section 4.1 and table 4.2 in section 4.3.2. The St of all the prescribed motion simulations are given in table 4.1. The amplitude of the pitch is varied. For this investigation the St values are chosen to mimic natural flappers with $St = 0.2 - 0.3$ [24]. It is noted that the spring simulation results shown in all of section 4.3 enabled the appropriate choice of pitch amplitude to attain optimal results. Without knowledge from spring simulations, a large prescribed motion design sweep would have needed to be performed.

The simulations fairly high angle of attack amplitudes (see θ_o values table 4.1) mimic the kinematics of biological flyers where natural flappers maintain efficiency.

For example, bats can fly and maneuver at angles of attack as high as $40^\circ - 60^\circ$.

4.2.1 Non-optimal simulations

First, prescribed motion simulations are performed with positive pitch amplitudes, ranging from 15° to 45° at $St = 0.127$. These flappers fail to produce thrust and are inefficient, only managing to generate large amounts of drag (see negative C_t values in table 4.1).

Their efficiencies are denoted by 0 in table 4.1, but actually the flappers are anti-efficient taking more energy from the flow than what is put in. In these simulations, the prescribed harmonic pitch misaligns the foil with respect to the flow, thus causing the massive separation/stall indicated by the large vortex generated on the foil

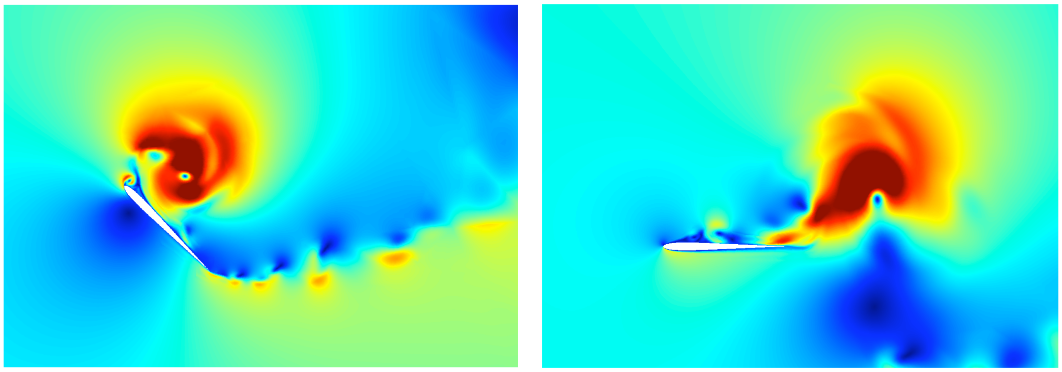

(a) $0.25T$ (b) $0.5T$

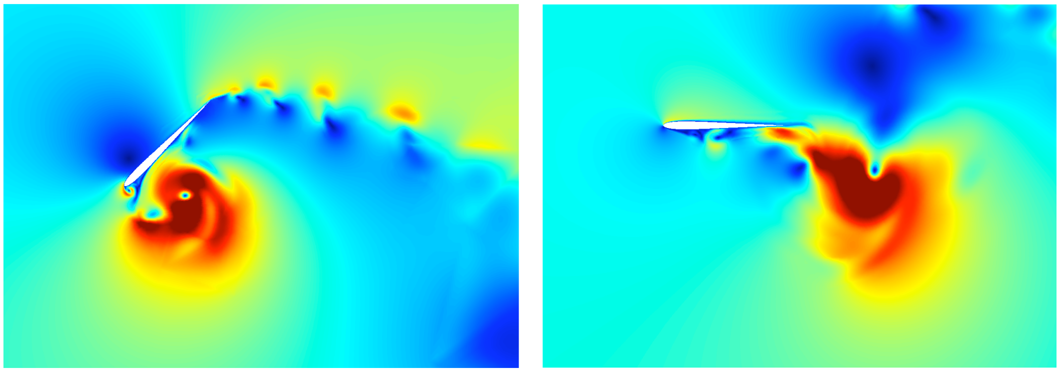

(c) $0.75T$ (d) T

Figure 4-2: Mach contours of prescribed motion, $\theta_o = 45^\circ$, $St = 0.127$. Mach contour scale 0 (blue) to 0.45 (red). This is clearly a very bad flapper but it illustrates the ability of the computational model to simulate off-design conditions accurately.

and then shed into its wake. However, these atrocious flapper simulations show the capability of code to accurately simulate harsh flow as seen in figure 4-2.

4.2.2 Optimal simulations

The negative amplitude cases, $\theta_o = -15°, -18°, -21.5°$ at $St = 0.2$ and $\theta_o = -45°$ at $St = 0.4$ are relatively good flappers, both generating significant thrust and all but $\theta_o = -15°$ are over 50% efficient (see table 4.1). These simulations are comparable with spring simulations presented later. For example, $St = 0.2$, $k = 0.4$ spring runs have η ranging between 0.3 and 0.5 and C_t ranging between 0.1 and 0.2 (depending on the spring stiffness). Also, the unsteady force plots in figure 4-3 depicts a relatively smooth force generation. Despite being efficient and thrust producing, the selected runs are a result of spring simulation knowledge.

Table 4.1: Prescribed oscillating foil simulations' coefficient of thrust and efficiency results. All simulations are run at $St = 0.127, 0.2, 0.4$ where $k = 0.4$, and $U = 1$. An efficiency of 0 means the airfoil generates drag not thrust indicating that it is anti-efficiency requiring more energy than the power input.

θ_o	St	C_t	η
15°	0.127	-0.3393	0
18°	0.127	-0.4576	0
21.5°	0.127	-0.5904	0
45°	0.127	-1.4638	0
$-15°$	0.2	0.1922	0.4195
$-18°$	0.2	0.1820	0.4931
$-21.5°$	0.2	0.1576	0.5618
$-45°$	0.2	-0.4602	0
$-45°$	0.4	0.3657	0.6780

4.2.3 Pitch profile dependency on Strouhal number

The $-45°$ pitch amplitude cases reflect the large dependence of the optimal pitch profile with respect to Strouhal. The $St = 0.2$ case is completely inefficient with drag coefficient over a period, 1.4638, whereas the simulation at $St = 0.4$ has a propulsive

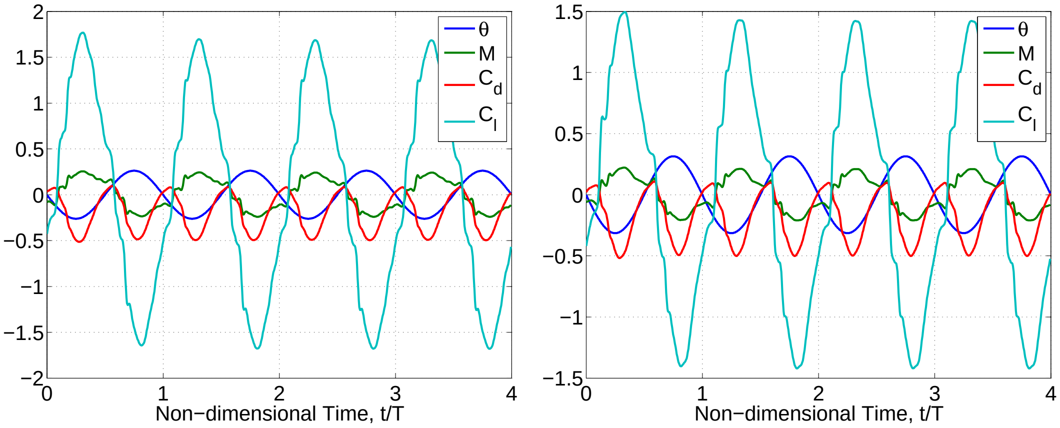

(a) $\theta_o = -15°$ (b) $\theta_o = -18°$

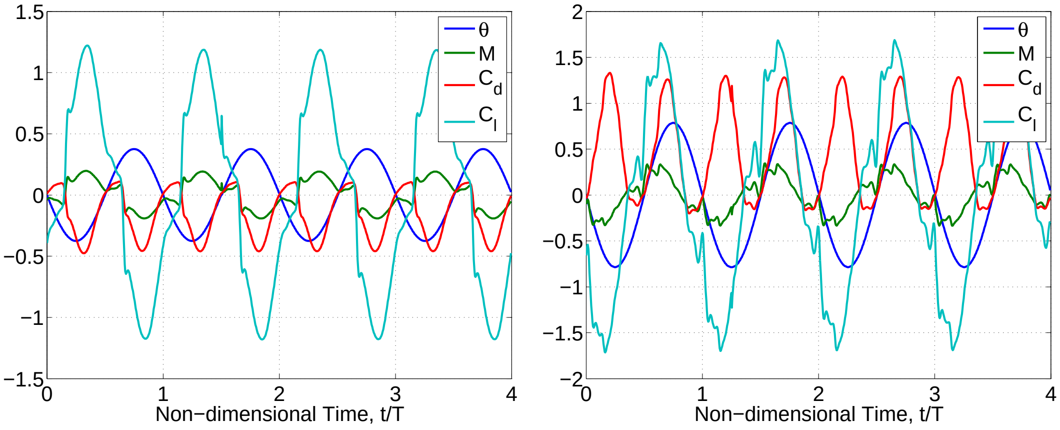

(c) $\theta_o = -21.5°$ (d) $\theta_o = -45°$

Figure 4-3: Time evolution plots of θ, M_f, C_d, and C_l for the prescribed foil simulations heaving at $St = 0.2$ with $\theta_o = -15°, -18°, -21.5°, -45°$. The pitch amplitudes, $\theta_o = -15°, -18°, -21.5°$ are consistent with the spring actuated airfoil at the same St number for a given spring stiffness.

efficiency of 0.757 and thrust coefficient of 0.3657. The extreme disparity is a result of the change in St number. By amplifying the St, the inertial flow effects are enhanced (accelerating more fluid) and thus the viscous separation forces become negligible (less of an important factor). Thus, the $St = 0.4$ simulation has minimal separation and therefore less erratic force generation. The occurrence and severity of separation is illustrated by the Mach contours in figure 4-4 for the low St case and figure 4-5 forthe high St case.

Also, figure 4-6 illustrates the polarity between the simulations unsteady force

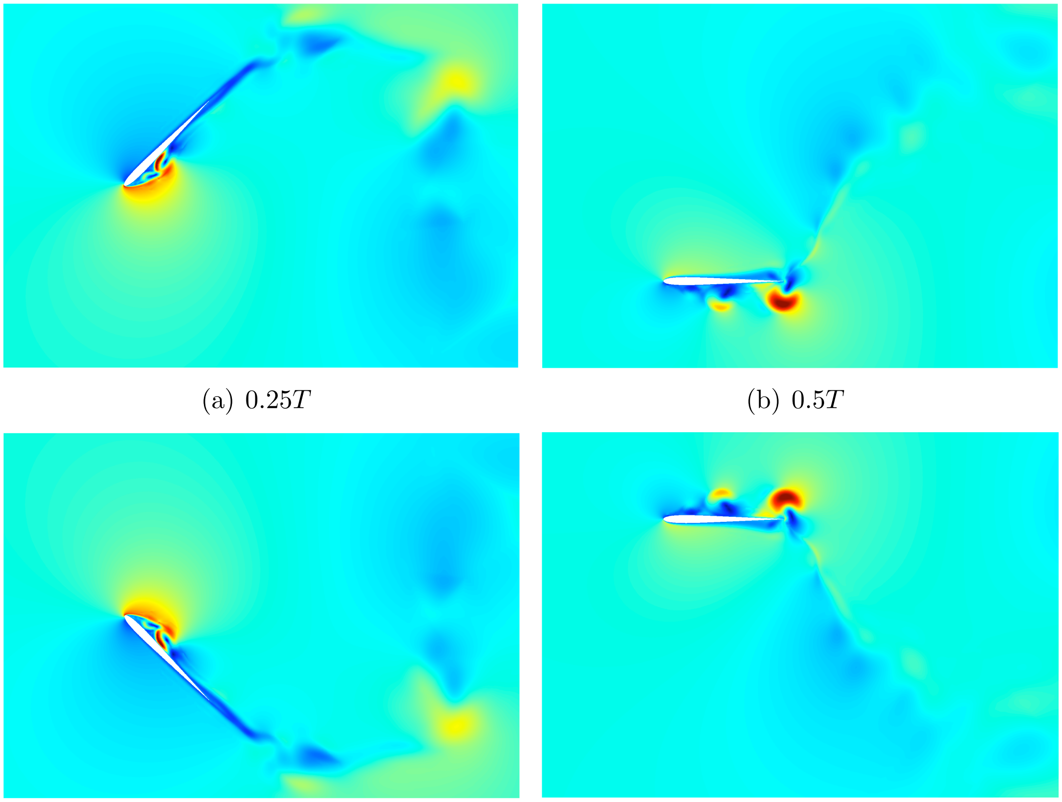
(a) $0.25T$ (b) $0.5T$ (c) $0.75T$ (d) T

Figure 4-4: Mach contours of prescribed motion, $\theta_o = -45°$, $St = 0.2$. Mach contour scale is 0 (blue) to 0.45 (red).

generation. Particularly, the variable behavior of the low St simulation signifies flow separation and propulsive inefficiency, whereas the regularity of force profiles for the high St simulation reflects a thrust-producing efficient flapper. However, this result only exemplifies the variation in pitch amplitude and fixes the pitch profile shape and lag with respect to heave.

4.2.4 Conclusions

Assuming the sinusoidal motion of the heave, the pitch dynamics must be more complicated to generate efficient, thrust producing flight especially when the pitch angle becomes large. Natural flappers sense input from the flow influencing their motion. Thus, it is suggested that adopting this biological flapping quality to guide designed flappers will elevate flight performance As seen from the prescribed motion

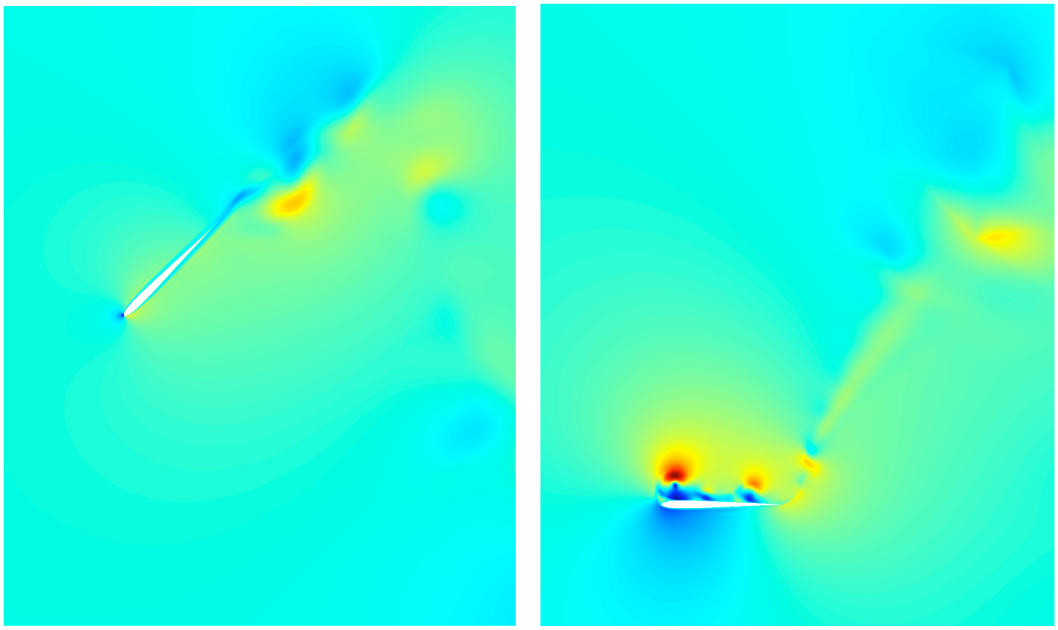

(a) $0.25T$

(b) $0.5T$

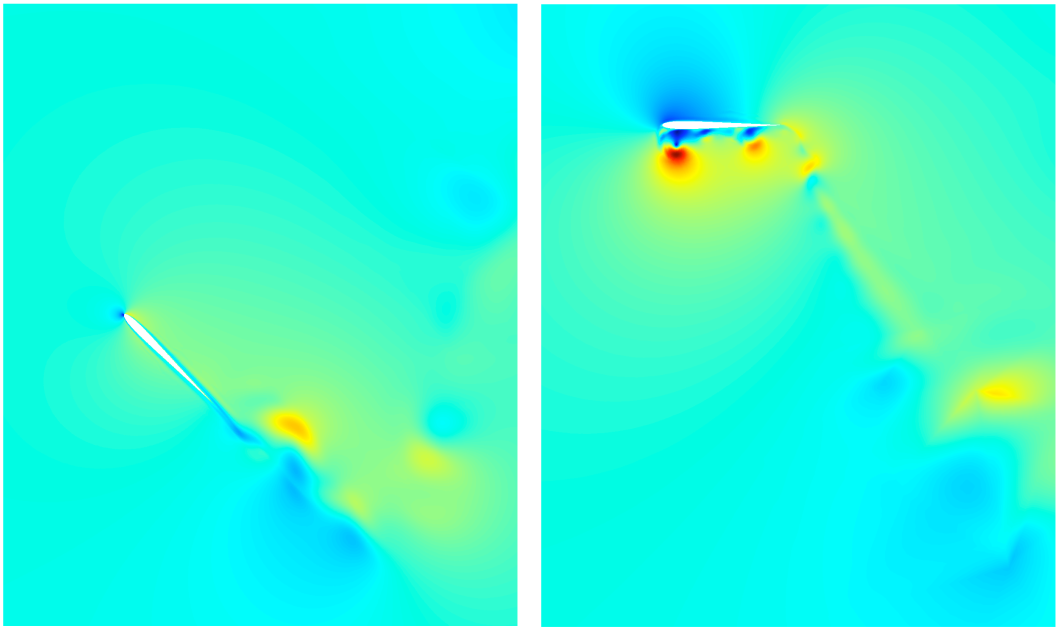

(c) $0.75T$

(d) T

Figure 4-5: Mach contours of prescribed motion, $\theta_o = -45°$, $St = 0.4$. Mach contour scale is 0 (blue) to 0.45 (red).

attempts, it is hard to set flapping motion and even generate thrust (seen from the non-optimal simulations performed). Furthermore, the inverse design for prescribed motion has an immense design space that involves too much trial and error.

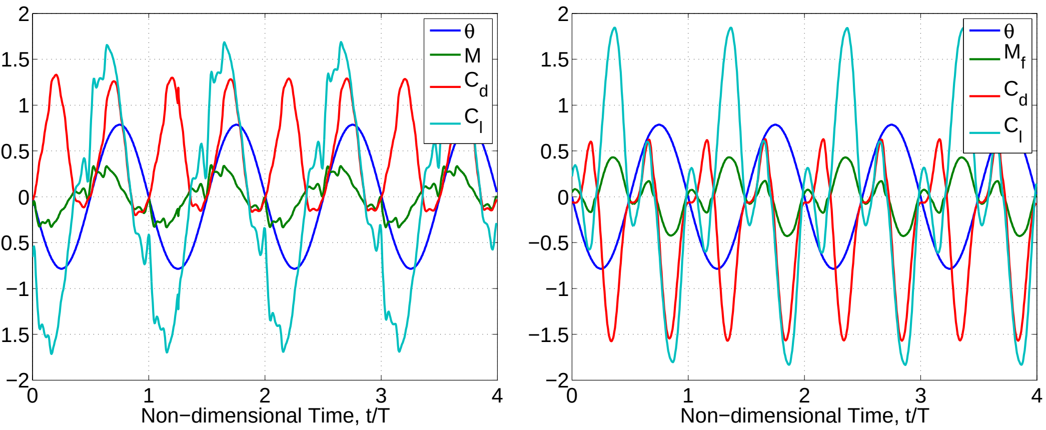

(a) $St = 0.2$, $\theta_o = -45°$

(b) $St = 0.4$, $\theta_o = -45°$

Figure 4-6: Time evolution plots of θ, M_f, C_d and C_l comparing $\theta_o = -45°$ pitch amplitude, heaving at both $St = 0.2$ (left) and $St = 0.4$ (right). This pitch amplitude is too large for the foil oscillating at $St = 0.2$. The foil expends energy to decelerate both its vertical motion and angular rotation to flip its angular orientation at the top and bottom of the heave. The foil heaving at lower St has less time to decelerate (due to lower heaving amplitude), thus it spends the majority of its transverse motion feathering, limiting its thrust generation during downstroke and exacerbating separation.

With prescribed motion, the optimal pitch angle amplitude is difficult to determine for an airfoil heaving at a specific St. The objective with the spring is to prescribe the heave but automatically determine the pitch angle modulation. Otherwise the determination of the effective pitch angle amplitude, lag, and periodic shape with respect to St would be the result of a massive prescribed motion design sweep i.e. sweep pitch angle amplitudes for each St and k combination and so on.

Thus, a new approach must be employed rather than just prescribed dynamics. In this thesis, a passive control model with a spring actuator uses the aerodynamic moment signal to generate desirable pitching. This approach removes a pitch amplitude, frequency, and phase parameters as a prescribed simulation input variable. The passive structural compliance to achieve appropriate pitch angles is inspired by the motion of natural flyers performing without adjusting their flapping cycle actively.

4.3 Passive spring actuation

The spring structural model is described in section 3.2.2 as well as the solution procedure for the simulations. The passive spring simulations involve design sweeps of several parameters.

4.3.1 Inverse strategy

Before attempting to investigate a model using a high fidelity code that takes considerable time to run an unsteady simulation, it is important to narrow a large design space using lower fidelity models that can quickly refine the parameter sweep to a reasonable size for computationally intensive codes.

This inverse strategy or bottom-up approach was exploited to rapidly provide insight into the flapping flight parameter space of this thesis. The entire computational framework and corresponding results are given in Willis et. al. [29],[31].

The lower fidelity codes are HallOpt [7], [8] ,[9], a wake only method and FastAero [30], a panel method. HallOpt predicts the wake (minimum power) vorticity distributions in a flapper's wake, thus determining approximations to how forces are generated efficiently. The method roughly estimates upper efficiency bounds of flapping flight, optimal frequency and amplitude of flapping. HallOpt initiates the formation of design space parameter dependence. A wake only analysis coupled with a structural inverse design determines an initial estimate for the spring constant. Now a flapping Strouhal number range and spring constant range are resolved for higher fidelity design sweeps. FastAero, a medium fidelity method (more accuracy but longer computation time), furthers the refinement of HallOpt requiring geometry information in a surface only, boundary element method to solve the potential flow equation [31]. This method does not model viscous flow but accounts for the unsteady motions, deformations and wake induced losses prevalent in flapping flight.

The inverse strategy enables the design of a feasible fluid structure interaction strategy. The wake only investigation indicates that efficient thrust production pertains to a specific range of Strouhal numbers which is quite similar to that observed in natural flyers [24]. Furthermore, the approximate 90° phase lead of heave with respect to pitch is determined to be optimal. The torsional spring at the leading edge of the rigid airfoil is an attempt to passively achieve the desirable phase shift between pitching and prescribed heaving (timing of flapping rotation) as well as general pitch behavior. To reiterate, the HallOpt preliminary prediction of the foil's leading edge spring constant narrowed the design space required for higher fidelity models. Then, the higher fidelity model in this thesis utilizes the refined design space with simulations that accurately describe the flow physics.

4.3.2 Design sweep

The simulations are performed setting the airfoil's moment of inertia $I = 0.033$ and mass moment about the pivot $S = 0.1 \approx I/0.3$ where $S = mx_{\mathrm{cg}}$. These values simulate a nearly massless airfoil. The description of the structural model is in section 3.2.2. The pitch and heave of the airfoil is characterized by a spring constant $C = I\omega_o^2$ where ω_o is the spring's natural frequency, and Strouhal number St from equation (4.1). These parameters as well as the aerodynamic moment affect the moment equation (3.6) which governs pitch response. The St number involvement is more subtle but it determines the $\ddot{h}$ term where $\ddot{h} = -\omega^2 h_o \cos\omega t$. The simulation commences with the airfoil configured at the top point of its heaving amplitude and at zero angle of attack.

Table 4.2: Definition and values/ranges of design space parameters of passively actuated oscillating foil simulations. The parametric space is refined using results from lower fidelity models.

Parameter	Definition	Value
St	Strouhal number	$[0.1, 0.5]$
C	spring constant	[0.1,0.5]
S	airfoil static imbalance	0.1
I	airfoil moment of inertia	0.033
ω_o	spring natural frequency	-
k	reduced frequency	$0.25, 0.4$
h	$h_o \cos\omega t$, heaving profile	-

Two 5×5 design sweeps were performed of the Strouhal number, St, and spring constant, C involving two reduced frequencies, $k = 0.25$ and 0.4. Table 4.2 lists the important parameters and quantity range (where appropriate) of the design sweeps.

Initially the design space sweeps were performed using explicit timestepping at $p = 3$; these results were redone with a finer mesh and a higher polynomial order, $p = 4$, using the implicit formulation yielding more accurate and resolved results.

The implicit simulations were run for 10 periods with 1000 timesteps per period. This time resolution was found to be necessary to capture all the high frequency effects present in many of the more extreme cases. The force generation stabilized between 3-4 periods of pitching and heaving. When separation occurs the average force over a period does not settle to a number but hovers around a particular efficiency. In these cases, an average of the efficiency and thrust for the last five periods of the simulation is used.

Order of magnitude analysis

With a simple order of magnitude perspective of the governing equation (3.6) linking the fluid and structure, one can hypothesize how the airfoil's kinematics will be affected by the flow. In particular, the moment balance in equation (3.6) gives the relation between the pitch angle and aerodynamic moment. There are four terms in this equation: $S\ddot{h}$, $C\theta$, M_f, $I\ddot{\theta}$. Looking at all the terms when they are at their greatest, the $\ddot{h}(t)$ term is known for each time step and is $O(10^{-2})$ to $O(10^{-1})$ depending on the case. The second derivative of θ reaches $O(1)$ only at the peak of θ when the derivative is drastically changing sign especially in a more triangular wave-like θ case. Despite this, the moment of inertia constant is small and the term is at most $O(10^{-1})$. On the other hand, the aerodynamic moment is $O(1)$ at least one order of magnitude greater than the $\ddot{h}$ term and $\ddot{\theta}$ term. Consequently, for the cases considered, we expect that the pitch angle behavior should somehow mimic the aerodynamic moment profile.

Effect of prescribed heaving

Both the Strouhal number and reduced frequency are non-dimensional parameters that characterize the heaving of the airfoil. Figure 4-7 depicts the heaving profiles generated for all Strouhal numbers in both reduced frequency design sweeps. As the St increases the amplitude of heaving grows illustrated in figure 4-7. The values of St with corresponding half-amplitude h_o are enumerated in Table 4.3.

The prescribed heaving has a strong effect on the pitch response of the leading edge spring. In the moment balance, thes aerodynamic moment term diminishes or compensates for a lower or higher $\ddot{h}$ term, respectively. Altering the moment generated by the fluid produces a different pitch angle. Consequently, a lower St number creates smaller pitch angle variation. Physically, a higher heaving amplitude (higher St) causes more displacement of fluid by the airfoil. This displacement effect is the primary factor in the magnitude of the pitch angle. This effect of Strouhal number on the pitch angle is characterized by the maximum pitch angle within a period, essentially the amplitude of the pitching motion. A high St results in a larger $\theta_{\max}$

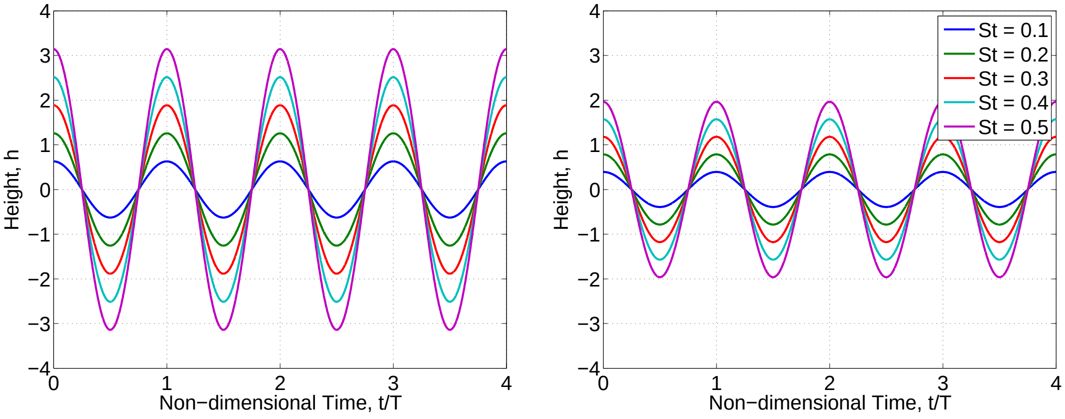

(a) $k = 0.25$ (b) $k = 0.4$

Figure 4-7: Illustration of the prescribed harmonic heaving profiles, $h(t) = h_o \cos(\omega t)$, for both reduced frequencies. The oscillating foil motion associated with a higher reduced frequency generates more acceleration of the flow (moving more quickly through the fluid). The acceleration-dominated flow displaces more fluid while plunging vertically and is thus the primary source of loading on the airfoil damping high frequency modes of viscous forces.

with slight discrepancies between the two reduced frequency cases. Table 4.3 gives the $\theta_{\max}$ values with respect to St. For low St, the maximum pitch angle is between $9-14°$ where the range shows the slight variation with spring stiffness. In general, the higher $\theta_{\max}$ in the range is a result of a mid-to-high spring constant (stiffer spring) within the design sweep. For large St numbers, the maximum pitch angle range is $50-56°$. Even at these extremely high angles of attack, the airfoil remains efficient and thrust-producing. The spring model enables the airfoil to maintain efficient flight due to its flow response (mainly reacting to the moment) mechanism letting pitch be regulated in time and not precisely determined beforehand.

Despite $\theta_{\max}$ remaining relatively consistent for a specific St independent of spring stiffness, the optimal pitch profile changes with St as well as C discussed in more detail in pitch angle analysis. Perhaps,the pitch angle is not the best indicator of the airfoil dynamic performance. Thus, we introduce the effective angle as the difference

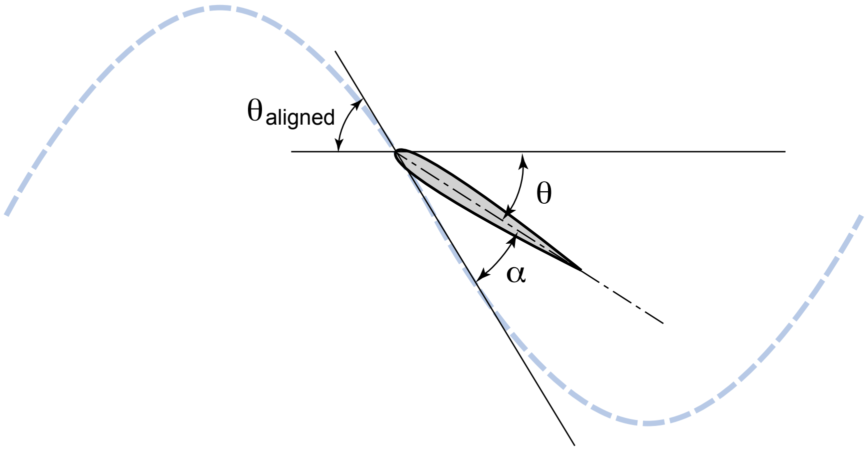

Figure 4-8: Schematic of the pitch angle, θ, the angle aligned with the flow θ_{aligned} and the effective angle α. The magnitude of the effective angle is a measure of the foils alignment with the flow path (foil motion through physical space) shown as the dotted light blue line. A high effective angle indicates less alignment and vice versa. Perfectly aligned flapping foils have minimal separation but do not produce thrust.

between the angle aligned with the flow and the pitch angle

$$\alpha = \theta_{\text{aligned}} - \theta \,, \tag{4.10}$$

where the angle aligned with the flow is

$$\theta_{\text{aligned}} = \arctan \frac{\dot{h}}{U} = \arctan \dot{h} \,. \tag{4.11}$$

A small effective angle means the airfoil is more aligned with the flow. Complete flow alignment of the oscillating foil represents a non-thrust mobilization. Thus, a very low effective angle produces non-separating flow but is not optimal in terms of efficient thrust production. The effective angle is in fact strongly dependent on all design parameters, C, St and k of the simulations. The α_{max} range with respect to St is detailed in table 4.3.

Table 4.3: The non-dimensional flapping frequency (St number) effect on the magnitude of the oscillating foil's angular motion in terms of pitch and effective angle. θ_{max} primarily depends on Strouhal number. Both θ_{max} and α_{max} are a range since they vary slightly across spring constants. The lowest maximum angle does not necessarily correspond to the smallest spring constant and vice versa. Also, the maximum pitch angle and effective angle remain fairly consistent for a single simulation with slight variation in the case of separation.

	$k = 0.25$			$k = 0.4$		
St	h_o	θ_{max}	α_{max}	h_o	θ_{max}	α_{max}
0.1	0.628	9°-14°	4.7°-8.3°	0.393	9°-14°	6.2°-8.4°
0.2	1.257	20°-28°	8°-14.3°	0.785 ($\pi/4$)	19°-27°	12°-18.9°
0.3	1.885	38°-40°	10.5°-17.7°	1.178	31°-37°	17.3°-28.4°
0.4	2.513	47°-49°	13°-27.9°	1.571 ($\pi/2$)	42°-47°	22.7°-34.8°
0.5	3.141 (π)	54°-56°	17°-33°	1.964	50°-55°	26.7°-35°

Time evolution characteristics of θ, M_f, C_d, C_l

At each time step, the pitch angle, moment, lift and drag are computed. These quantities reflect the airfoil dynamics and force production behavior within the parametric

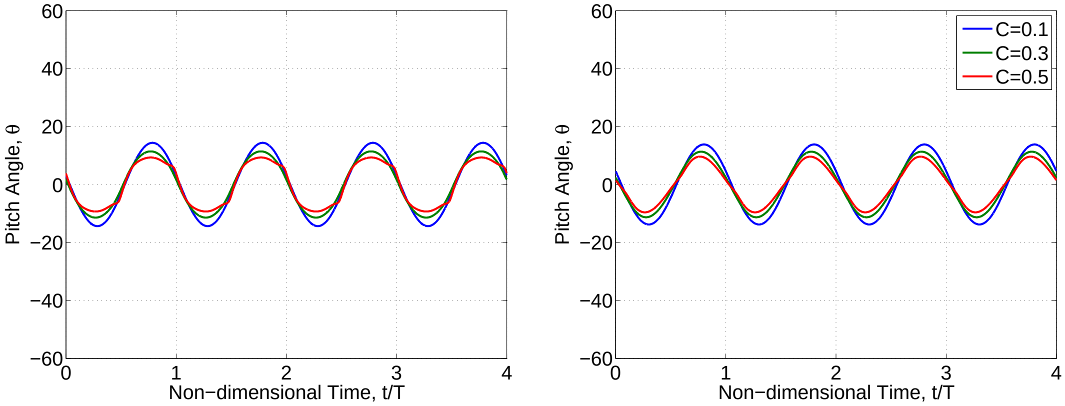

(a) $k = 0.25,\ St = 0.1$ (b) $k = 0.4,\ St = 0.1$

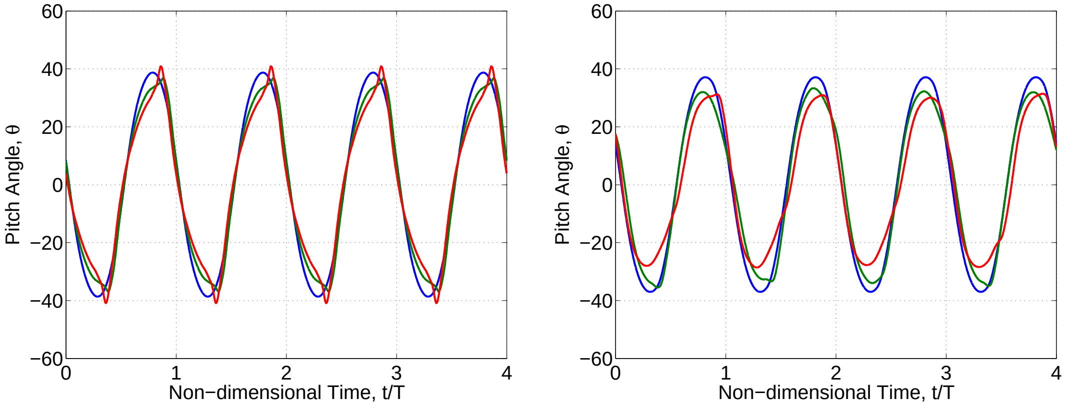

(c) $k = 0.25,\ St = 0.3$ (d) $k = 0.4,\ St = 0.3$

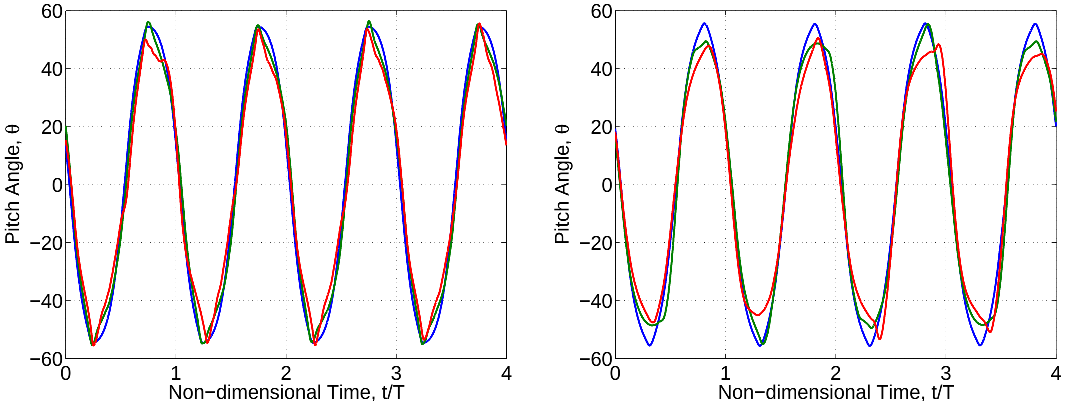

(e) $k = 0.25,\ St = 0.5$ (f) $k = 0.4,\ St = 0.5$

Figure 4-9: Simulation results for the passively actuated pitch angle of the oscillating foil. The Strouhal number mainly affects the amplitude of the pitch. A high St allows the foil to attain a higher $\theta_{\max}$ while accelerating around mid-heave. The spring stiffness signifies the magnitude of the foil's resistance to the aerodynamic moment of the fluid. A stiffer spring (higher C) for a given St number increases the likelihood of the occurrence of separation. A less sinusoidal pitch modulation suggests the presence of separating flow.

space. Also, the time-varying behavior allows the interpretation of flow effects, i.e. viscosity, inertia, etc ..., with respect to the design parameters, St and C.

Solely looking at the pitch angle in figure 4-9, the sampling of design sweep profiles depicts a pitch profile shape trend in the design space; this shape can be interpreted as a signal of stall or separation onset. At low St as seen in figure 4-9(a) and 4-9(b), the pitch has a sinusoidal shape especially for $C < 0.3$. For St in the mid-range of the parametric sweep (figure 4-9(c) and 4-9(d)), a harmonic time-varying pitch angle occurs for lower C or softer springs; however, for stiffer springs the peak of the curve sharpens. In other words, the pitch is no longer behaving as a sinusoid but takes on more triangular wave pattern. The peak sharpening occurs with softer spring-driven oscillating foils more often for the lower reduced frequency than for a higher reduced frequency. For example, at $St = 0.3$ sharpening in the pitch curve appears as early as $C = 0.3$ for $k = 0.25$, a relatively soft spring; on the other hand, in the $k = 0.4$ sweep at $St = 0.3$ noticeable triangulation begins only at $C = 0.5$ with a very stiff spring. A higher reduced frequency signifies quicker acceleration of the fluid (smaller period of oscillation) which may damp out some of the high frequencies in the θ signal causing this discrepancy. Thus, the mismatch with respect to the comparison of θ behavior of the different reduced frequency cases infers that the pitch angle behavior is dependent on both the k and St; thus, any comparisons of pitch angle need to take in account both parameters. Despite this, in general as the heaving amplitude grows, the pitch angle evolves as a triangular-like wave regardless of the magnitude of C seen in the high St cases in figure 4-9(e) and 4-9(f).

The progression from a sinusoidal pitch angle time evolution to a more triangular, asymmetric wave signifies a change from fully-attached flow to separated flow and even stall. In fact, just the asymmetric behavior in the pitch angle can be used as an indicator of undesirable flow separation. Generally, separation is more frequent at a lower reduced frequency since the amplitude of the heave is higher for the same St than in a higher reduced frequency simulation i.e. for $St = 0.3$, $k = 0.25$ has the heaving amplitude $h_o = 1.885$ whereas $k = 0.4$ has $h_o = 1.178$ (more examples in table 4.3). The amplified heaving increases the chance of separation and stall.

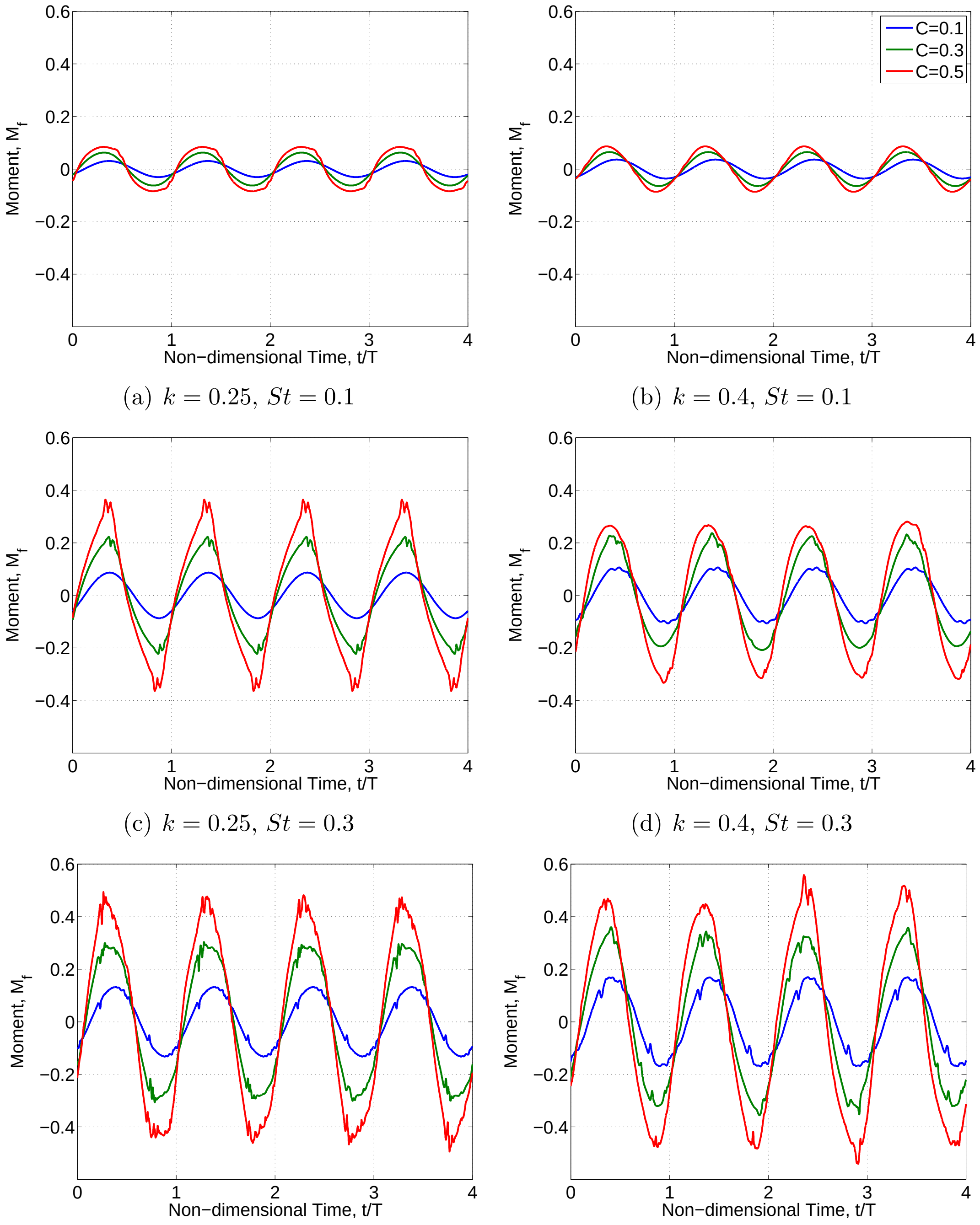

(a) $k = 0.25$, $St = 0.1$

(b) $k = 0.4$, $St = 0.1$

(c) $k = 0.25$, $St = 0.3$

(d) $k = 0.4$, $St = 0.3$

(e) $k = 0.25$, $St = 0.5$

(f) $k = 0.4$, $St = 0.5$

Figure 4-10: The time-varying aerodynamic moment, M_f, primarily drives the foil angular motion. When separating, the torque needed to flip the angular rotation of the foil is large due to the suction on the airfoil surface.

Nonetheless regardless of the Strouhal number, a stiff spring increases the chance of viscous separation. Even the $St = 0.1$, $C = 0.5$ cases have slight asymmetry in the pitch profile reflecting slight flow detachment from the foil. Separation manifests itself when the airfoil is misaligned with the flow and most often occurs at the top and bottom of the heaving cycle as the airfoil is decelerating and feathering. A stiffer spring inhibits the airfoil's propensity to conform to the fluid motion and align with the flow, thus causing separation. Although a perfectly aligned oscillating foil does not separate, it produces minimal forcing, performing inefficiently. Furthermore, there is a tradeoff between separation minimization and force generation.

As predicted or asserted in the order of magnitude analysis, the moment primarily drives the pitch angle; thus, the moment and pitch have similar trends. The time evolution moment plots are in figure 4-10. The moment is slightly different from θ in that the amplitude of the curve increases as the spring stiffens especially with more vigorous flapping (high St), inferred from figures 4-10(e) and 4-10(f)). As with the pitch angle, the moment behavior is less smooth and more triangular at its peaks for higher C, $St > 0.2$, and more noticeably with $k = 0.25$.

In addition, the moment behavior indicates separation and stall more noticeably. The peaks of the moment profile fluctuate up and down slightly, whereas the pitch angle tends to be more smooth. This discrepancy is due to the fact that the moment is a signal directly from the fluid and thus less well-behaved. The small vacillations of the moment are damped out in the pitch response. The small filtering/smoothing of the pitch angle is a results of the $\ddot{h}$, $\ddot{\theta}$ terms of the moment balance. Even though these terms are small compared to the moment (as shown in the order of magnitude analysis), they remove the high frequency component of the moment signal leading to the smoother pitch angle profile.

Figures 4-12 and 4-13 depict the forces generated in terms of their coefficients C_d and C_l, respectively, defined in (4.3). The moment is a linear combination of the drag and lift described by equation (3.13) and thus displays the same behavior of D and L with respect St, C, and indication of separation/stall. These forces are essential for the thrust and efficiency computations described in detail later in this section. Briefly, the drag represents the thrust generation of the foil where the thrust is in the opposite direction to drag. The spring performs remarkably well with

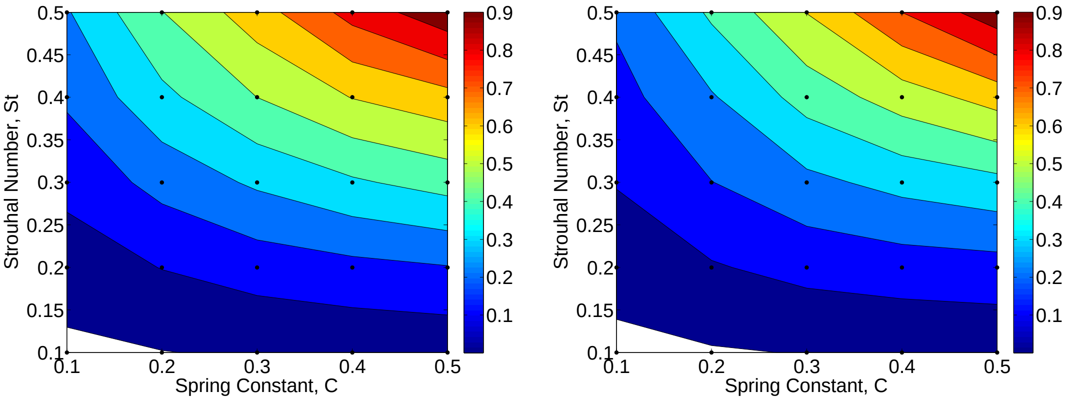

(a) $k = 0.25$ (b) $k = 0.4$

Figure 4-11: The coefficient of thrust, C_t, contours are relatively the same for both reduced frequency sweeps. In particular, a large heaving amplitude and stiffer spring produces the most thrust. Generally, a higher St number enables the airfoil to generate more thrust, since the foil spends a longer time at a high angle of attack on the downstroke. Also, more thrust occurs with a stiffer spring as the foil has less of a propensity to align with the flow; however, if the spring becomes too stiff the additional thrust is not advantageous due to efficiency reduction from separation.

time-varying thrust coefficient values reaching $C_t(t) = 2$ and even greater in certain high St, stiff spring cases. The average thrusts across a period for both reduced frequency design sweeps are shown in figure 4-11. The spring can generate $C_t > 0.7$ (over a period) with imprecise motion whereas a prescribed flapping foil needs an optimized pitch profile found after design iterations to acquire the same thrust. The thrust relates to the work produced by the airfoil. A stiffer spring and higher St number amplify thrust generation. Nonetheless, there is a threshold of the St and C where the enhanced thrust is at the cost of efficiency due to aggravated separation. This energetics tradeoff implies the oscillating foil has to balance inertial and viscous forces. Thus, the viscous (separation) forces need to be negligible in contrast to the increased loading on the foil from displacing the fluid, otherwise the separation losses reduce the foil's propulsive efficiency.

The lift is an indication of the work put into the dynamical system. For high St, high C cases the C_l reaches 2 within a period; once again quantifying the effectiveness of the spring model. In addition, despite the presence of harsh flow structures,

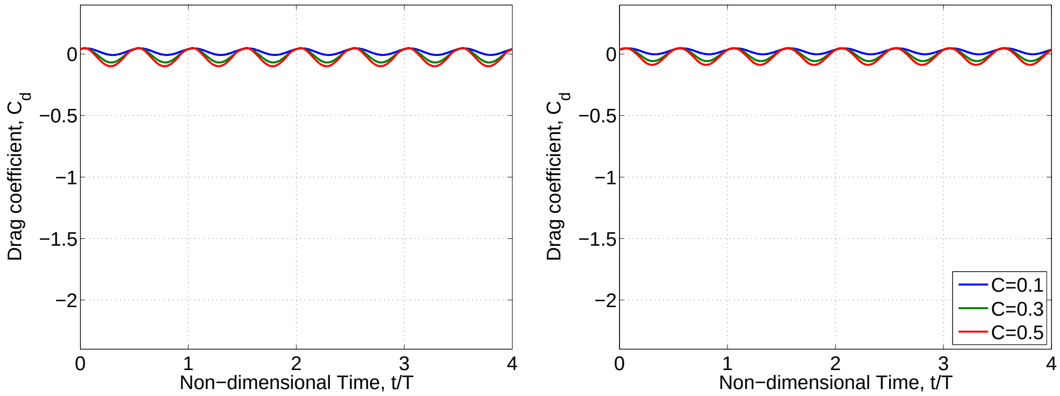

(a) $k = 0.25$, $St = 0.1$ (b) $k = 0.4$, $St = 0.1$

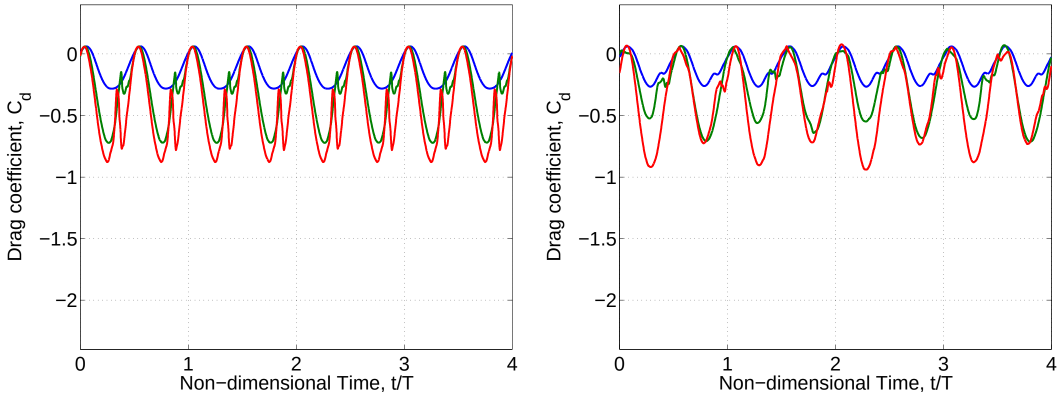

(c) $k = 0.25$, $St = 0.3$ (d) $k = 0.4$, $St = 0.3$

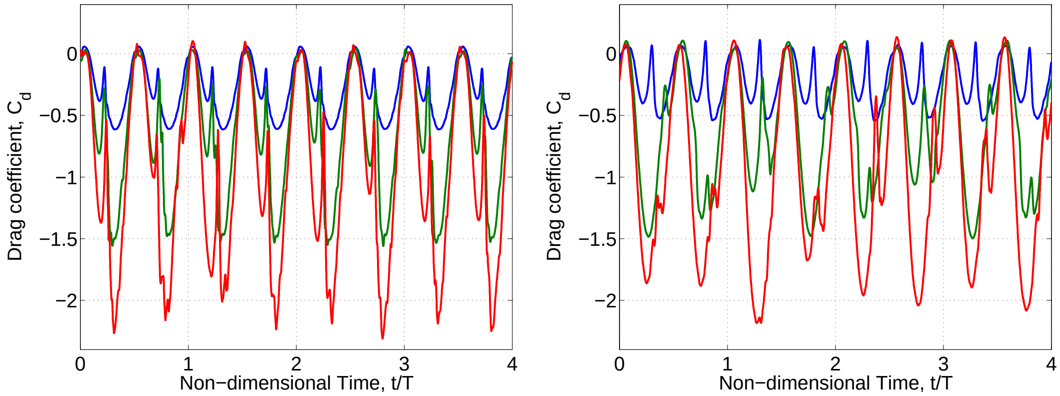

(e) $k = 0.25$, $St = 0.5$ (f) $k = 0.4$, $St = 0.5$

Figure 4-12: Plots of the time-varying drag coefficient results for both reduced frequency sweeps at various Strouhal numbers and spring stiffnesses. As the airfoil changes directions both vertically and rotationally, separation causes more erratic unsteady force generation. At higher St and C, the variable drag is present somewhat throughout the foil's oscillation cycle.

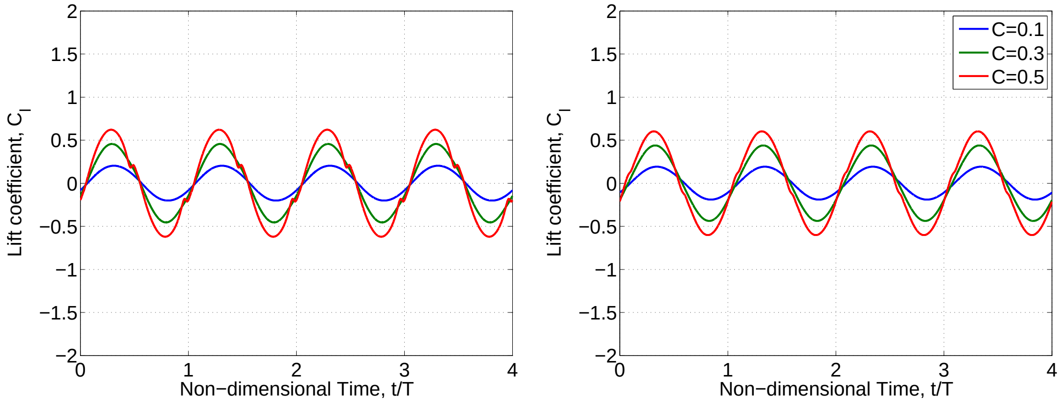

(a) $k = 0.25,\ St = 0.1$ (b) $k = 0.4,\ St = 0.1$

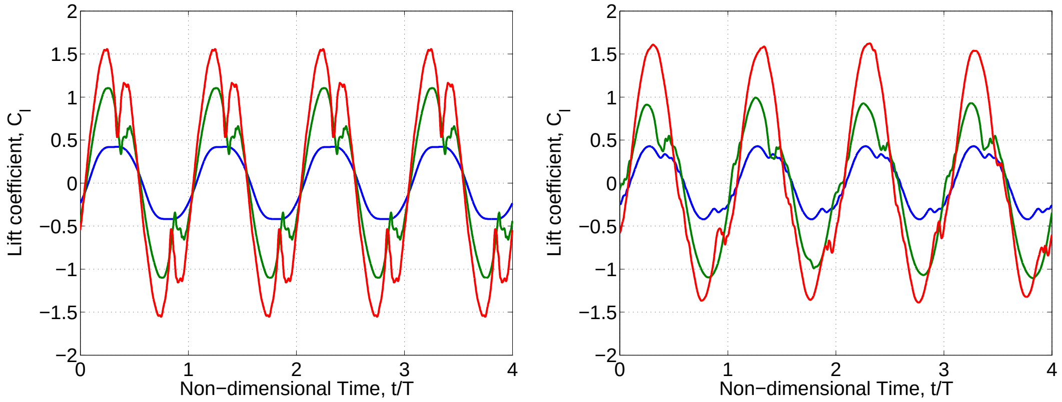

(c) $k = 0.25,\ St = 0.3$ (d) $k = 0.4,\ St = 0.3$

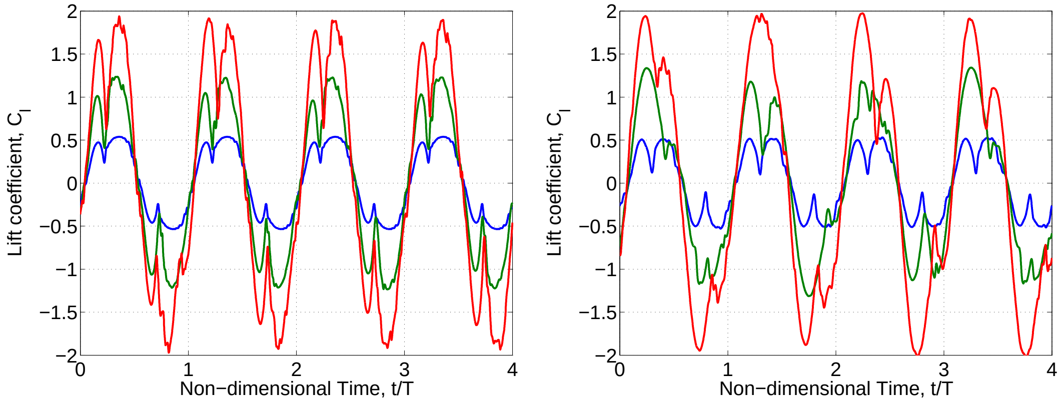

(e) $k = 0.25,\ St = 0.5$ (f) $k = 0.4,\ St = 0.5$

Figure 4-13: The unsteady lift coefficient is plotted. The time-averaged lift is a factor of the work inserted into the dynamical system.

the force generation manages to remain fairly regular since inertial forces are substantially larger than viscous forces (damping of high frequency modes in flow). The reactive spring model outperforms the prescribe motion cases with more regular force generation and actual thrust production.

Table 5.1 summarizes and quantifies the aforementioned trends with respect to the design parameters. For a complete analysis, the pitch angle and effective angle behavior are further assessed.

Pitch angle analysis

The maximum pitch angle, $\theta_{\max}$, and max effective angle, $\alpha_{\max}$, trends across the design sweeps are depicted in figure 4-14 and 4-15. The maximum effective angle occurs when the oscillating airfoil is at mid-heave plunging downward or upward at its maximum pitch angle (in the absolute sense i.e. magnitude).

The pitch angle amplitude is almost purely dependent on St and independent of the spring stiffness as previously mentioned in the effect of prescribed heaving trends. On the other hand, the effective angle has nearly a linear dependence on both St and C i.e. as the St and C increase, $\alpha_{\max}$ is larger and vice versa. This proportional behavior is true for the entire $k = 0.25$ design sweep. Thus, for softer springs and lower amplitude heaving, the airfoil is more aligned with the flow (lower $\alpha_{\max}$). However, for the $k = 0.4$ a separation dependency also becomes a factor for high amplitude heaving ($St > 0.3$) and stiff springs ($C > 0.3$). Despite the occurrence of separation, high amplitude heaving flappers experience loading predominately due to acceleration of fluid mass. This massive displacement of fluid is the major contributor of thrust generation. Consequently, a high effective angle is not just an indicator of separation, but is correlated with thrust i.e. high effective angle signifies high thrust. Furthermore, regardless of separation the accelerated-dominant flow is efficient since viscous forces are damped by large inertial forces. Hence, effective angle is an indicator of efficiency as well. As seen in figure 4-15(b), the plot has a bucket of high $\alpha_{\max}$ similar to the sweep's efficiency contour indentation (or dip) of high efficiency shown in figure 4-22(b).

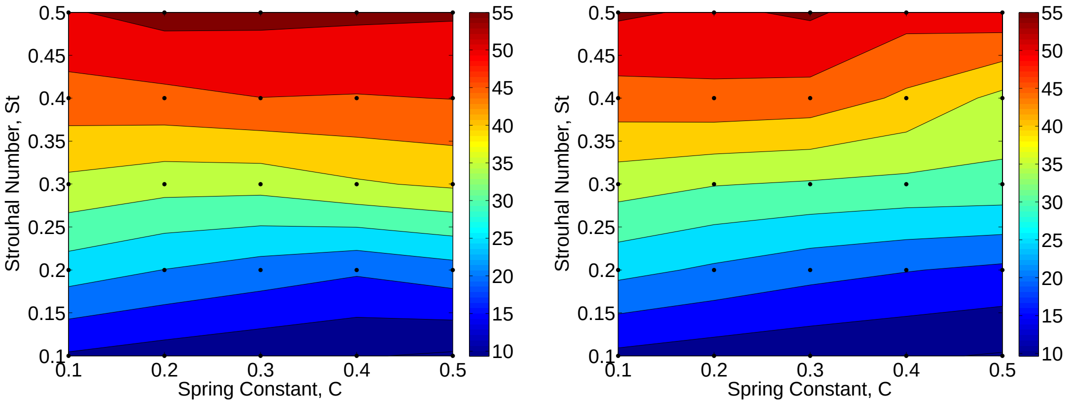

(a) $k = 0.25$ (b) $k = 0.4$

Figure 4-14: The maximum pitch angle variation (contours) is shown over the parametric space and is found to be largely St dependent.

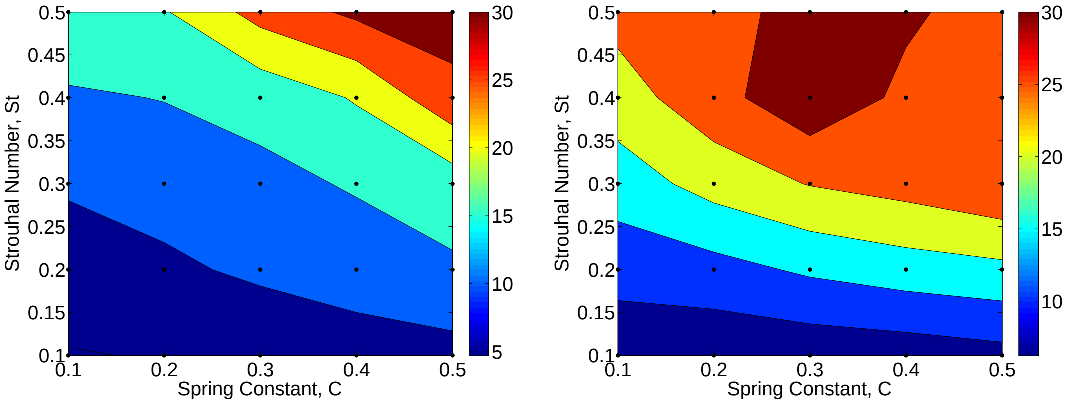

(a) $k = 0.25$ (b) $k = 0.4$

Figure 4-15: The maximum effective angle variation is depicted as contours over the design space. For the lower reduced frequency (left), the maximum effective angle has a positive, linear correlation with both St and C. The same is true in the higher reduced frequency design until $St > 0.4$ when separation effects alter the flapper kinematic behavior. Interestingly, the maximum effective angle contour begins to resemble the efficiency contour in figure 4-22(b).

In addition to the $\theta_{\max}$ behavior, the entire pitch angle response ($\theta(t)$) has a specific shape for every design point. To characterize the pitch response with respect to time, a sine wave is fitted to the pitch angle data in which the fitted analog is

$$\theta_{\text{fit}} = \theta_A \sin(\omega t + \phi) \tag{4.12}$$

where θ_A is the amplitude, ω is the frequency, and ϕ is the phase lag. The Levenberg-Marquardt algorithm [20, 12, 11] is employed to perform a least square curve fit of the pitch angle profile. The approach is a sinusoidal least squares (SLSQ) routine detailed in appendix B.

Figure 4-16 reiterates the trends previously described for θ. The pitch profile is modeled well by a sinusoid for softer springs. Figure 4-17 quanitfies the deviation of θ_A and $\theta_{\max}$ where the sine fit generates the most error. Also supporting the sinusoidal pitch behavior for soft springs is the L2-norm, $\|\theta(t) - \theta_{\text{fit}}(t)\|$, shown in figure 4-18.

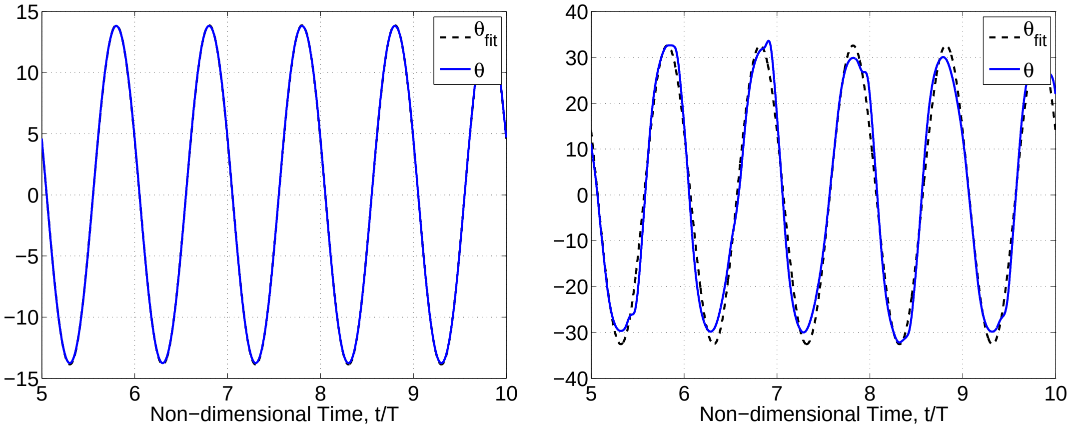

(a) $k = 0.4$, $St = 0.1$, $C = 0.1$ (b) $k = 0.4$, $St = 0.3$, $C = 0.4$

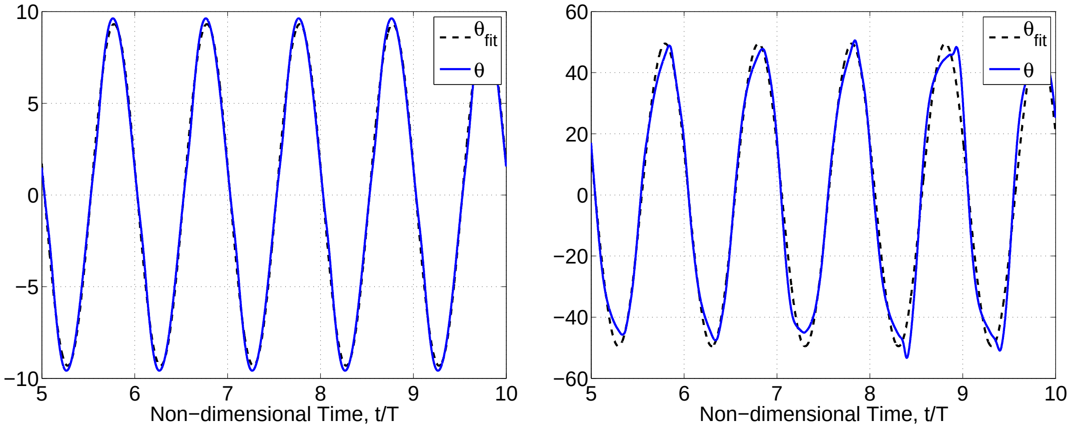

(c) $k = 0.4$, $St = 0.1$, $C = 0.5$ (d) $k = 0.4$, $St = 0.5$, $C = 0.5$

Figure 4-16: The fitted sine θ_{fit} and the pitch angle θ are plotted together in degrees for four simulations. The sinusoidal fits: 4-16(a) $\theta_{\text{fit}} = -13.8 \sin(0.8t - 18.9)$, 4-16(b) $\theta_{\text{fit}} = -32.6 \sin(0.8t - 25.9)$, 4-16(c) $\theta_{\text{fit}} = -9.3 \sin(0.8t - 11.3)$, 4-16(d) $\theta_{\text{fit}} = -49.5 \sin(0.796t - 7.1)$.

The L2-norm area depicts the variation from a harmonic along the entire profile of the pitch angle.

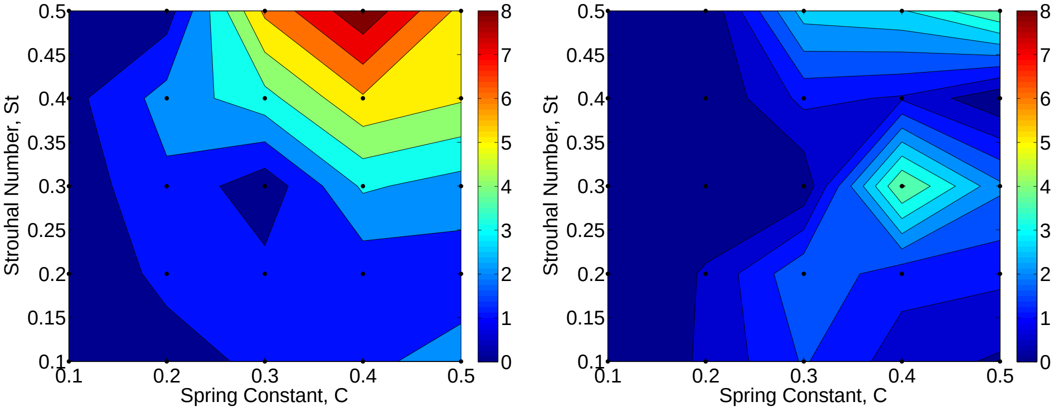

(a) $k = 0.25$,

(b) $k = 0.4$

Figure 4-17: The contours portray the difference between the fitted sine amplitude θ_A and the pitch angle amplitude $\theta_{\max}$ for both design sweeps. A more vigorous flapping, stiffer foil's pitch deviates the most from harmonic motion.

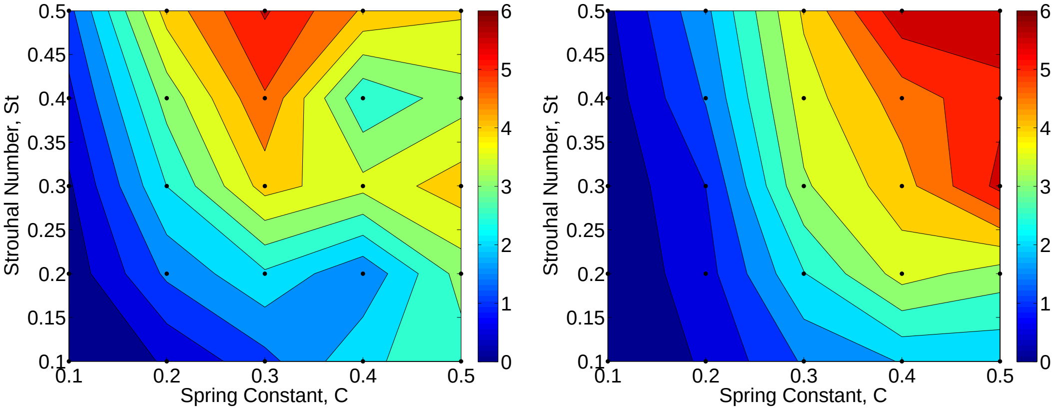

(a) $k = 0.25$

(b) $k = 0.4$

Figure 4-18: The contours depict the L2-norm between the fitted sine θ_{fit} and the pitch angle, $\|\theta - \theta_{\text{fit}}\|$. As the passively actuating spring becomes stiffer and heaving amplitude increases, the oscillating foil's pitch becomes less sine-like due to viscous effects.

Lag between moment and pitch

By fitting sinusoids to both the moment and pitch angle, the phase lag (between M_f and θ) is computed. The fitted harmonic is determined as previously using the Levenberg-Marquardt algorithm. The spring does not prescribe a particular lag; it is more reactive adjusting depending on the design location. Figure 4-19 has the design sweep contours of the M_f, θ lag. All the lags are between 160° and 230°. Also, the phase lag decreases for a airfoil heaving at a higher St. The lag variation across C is minimal for the low reduced frequency design, whereas the higher reduced frequency cases have slightly more deviation with respect to spring stiffness. In general $k = 0.25$ sweeps have higher lags compared to the $k = 0.4$ sweep. These lag variations could be a result of Theodorsen lag [25] effects or separation effects. Lastly, stronger viscous effects (present in high St and high C flappers) trigger earlier pitch angle decline or reduction signified by lower phase lag of the pitch angle with respect to the aerodynamic moment..

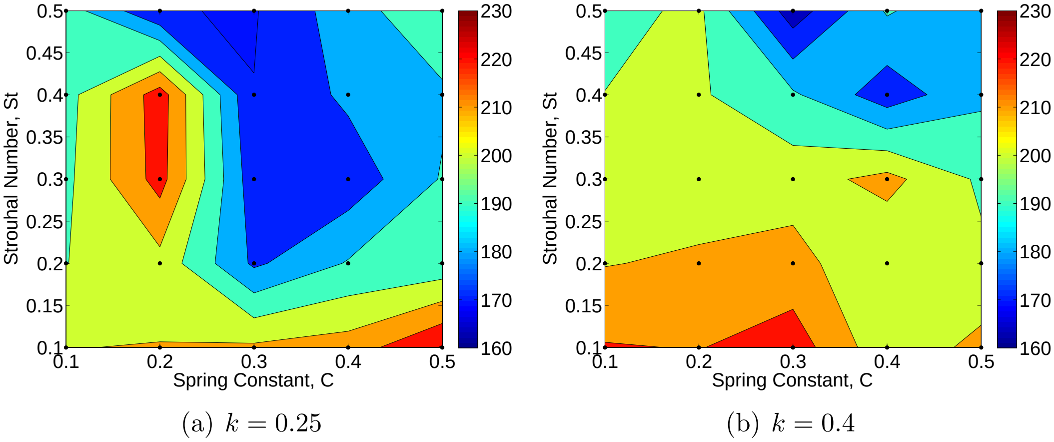

(a) $k = 0.25$

(b) $k = 0.4$

Figure 4-19: The phase lag of the pitch angle with respect to the aerodynamic moment varies between 160° and 230°. The lag is inversely proportional to Strouhal number and spring stiffness. Thus indicating that the presence of separation (in the higher St, larger C simulations) causes the pitch angle to reach its maximum value earlier.

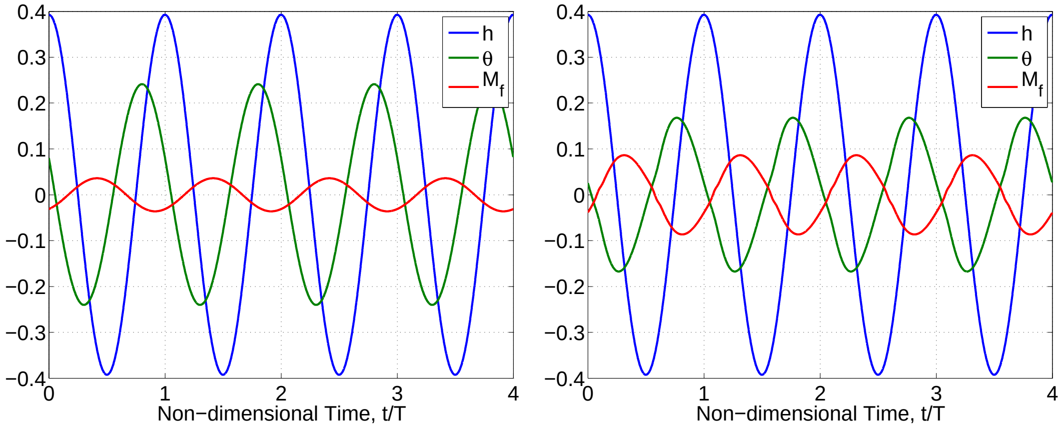

(a) $k = 0.4$, $St = 0.1$, $C = 0.1$ (b) $k = 0.4$, $St = 0.1$, $C = 0.5$

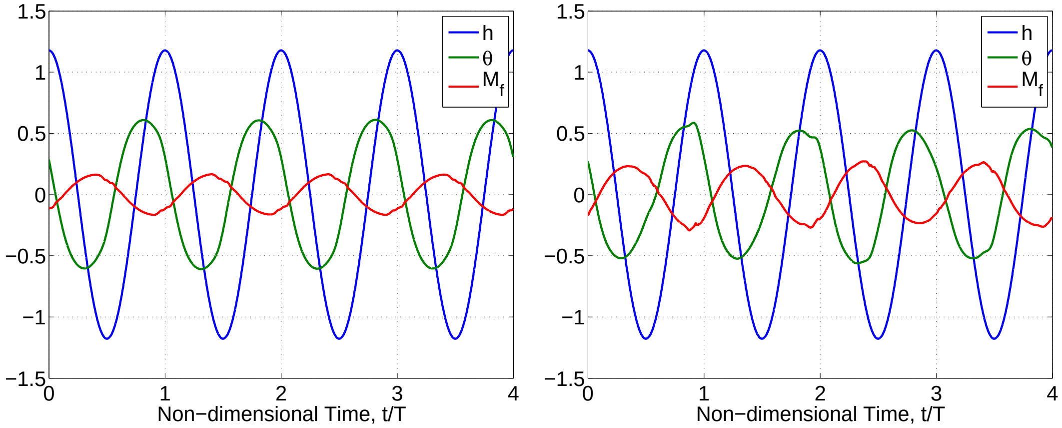

(c) $k = 0.4$, $St = 0.3$, $C = 0.2$ (d) $k = 0.4$, $St = 0.3$, $C = 0.4$

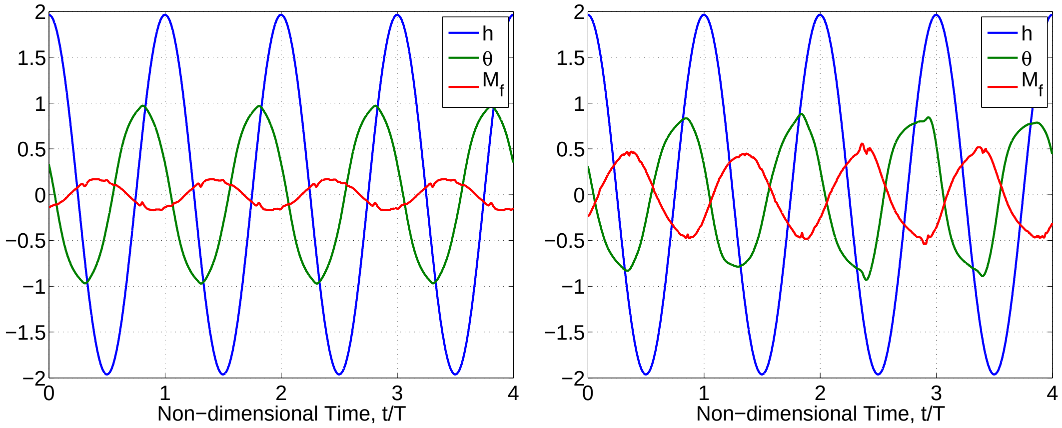

(e) $k = 0.4$, $St = 0.5$, $C = 0.1$ (f) $k = 0.4$, $St = 0.5$, $C = 0.5$

Figure 4-20: Heave, pitch angle, and moment over time are shown. Note that in this case θ is plotted in radians. Also the top row and bottom row of the figure are plots of the extrema of the $k = 0.4$ design sweep, whereas the middle row depicts two moderate cases (in the mid-range of the sweep parameters).

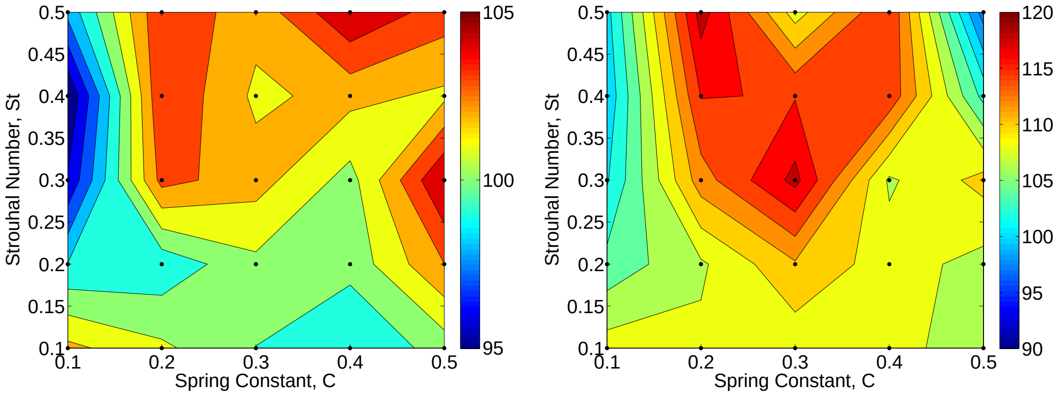

(a) $k = 0.25$ (b) $k = 0.4$

Figure 4-21: The heave motion has a phase lead with respect to the pitch. Phase values are depicted in the contours. The spring model generates phase angles, ϕ, around the asserted ideal of 90° with slight more variation across the parametric space for the higher reduced frequency sweep. It appears that lower phase lags occur for softer springs when separation is less prevelant.

Ideal lag between pitch and heave

The lag between the pitch and heave motion is an essential contributor in a efficient, thrust producing flapper. Ideally, it is asserted that an approximately 90° phase lag is optimal; thus, all the prescribed oscillating foil simulations from section 4.2 are performed with a 90° lag. As seen from the moment-pitch angle lag, separation inhibits the pitch angle from increasing. Thus, just before separation the pitch angle reaches a maximum and creates the lag with the heave. As the airfoil is in its upstroke or downstroke, the pitch angle maximum (or minimum) occurs approximately at mid-stroke ($h = 0$) before it begins to slow down for an eventual change in direction.

Figure 4-21 shows the heave-pitch lag for all design points of the two reduced frequency design sweeps. The low reduced frequency sweep has a small lag range of $[95°, 105°]$ in which low St, high C or high St, low C simulations have smaller lags and vice versa. The lower lags seem to correlate with simulations of non-separating flow. In other words, when θ behaves harmonically, the lag tends toward 90°. For the higher reduced frequency sweep, there is a larger lag range of $[90°, 120°]$. The range of high lag values occurs when $C = 0.2 - 0.4$ and $St = 0.2 - 0.5$ which in general is

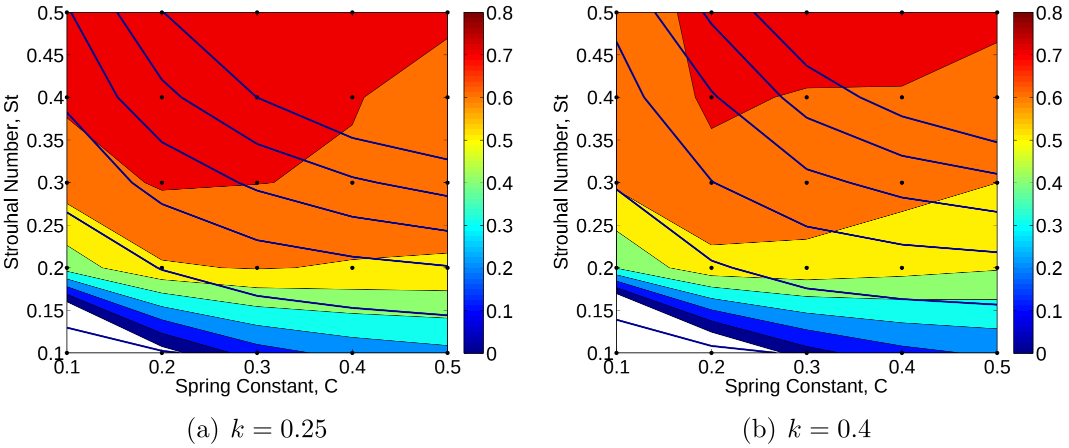

(a) $k = 0.25$

(b) $k = 0.4$

Figure 4-22: The contours represent the propulsive efficiency of the oscillating foil while the superimposed lines indicate constant thrust. For a given spring stiffness, the most efficient flapping strategy is determined by finding the region along a line of constant thrust at which the flapper's efficiency is optimized.

when separation is more likely indicated by wavering present in pitch angle profiles.

Efficiency and thrust analysis

Both the propulsive efficiency and coefficient of thrust defined in equations (4.8) and (4.5), respectively, are computed and shown in figure 4-22. This computation ignores dynamic effects since the airfoil model is essentially massless.

The spring driven airfoil remains relatively efficient for $C > 0.3$ i.e. has a huge range of efficient flight. This large efficiency range indicates that one can select a spring stiffness and then have a variable amplitude flapper without losing propulsive efficiency. Also, for a specific thrust requirement, the optimum spring constant and Strouhal which gives the maximum efficiency can be easily pinpointed by running along a line of constant thrust in figure 4-22. For lower thrust requirements, this maximum efficiency point is for low St, low spring constant oscillating foils, while higher thrust requirements demand more active flapping and a stiffer spring. Even though the low St flappers do not experience separation, they do not generate enough thrust to be efficient. Also, despite slightly advantageous thrust generation for a higher spring constant parameter, as the C increases the likelihood of stall also increases. When the airfoil stalls, there is a reduction in efficiency. At high St, the inertial loading on the airfoil still remains predominant, counteracting separation effects. Consequently, higher heaving amplitude flappers still attain very efficient, thrust-producing flight despite separation effects.

Although a perfectly aligned oscillating foil does not separate, it produces minimal forcing, performing inefficiently. As the foil plunges downward at a large negative pitch angle, the magnitude of its effective angle determines the amount of thrust generated i.e. larger α than more thrust. However, at the bottom of the heave cycle, the separation is a result of the foil's deceleration and angular rotation. With a stiffer spring, the foil has more resistance to change in vertical direction and torquing resulting in a higher tendency of separation. However, separation is not an indicator of inefficient performance. As long as the thrust production in the downstroke overcompensates for the separation losses at the top and bottom of the heaving cycle, the oscillating foil is an efficient flapper.

Importantly, the separated flow is correctly modeled in this high fidelity model and thus, it predicts this flow regime accurately. In conclusion, the design sweeps carried out with our DG code simulate an efficient, passive two-dimensional thrust generation model.

Inertial vs viscous force discussion

The loading on the airfoil is the product of the unsteady inertial forces and viscous (separation) forces. The inertial forces are acceleration dominated. If the reduced frequency is sufficiently high, the viscous effects become negligible, and the majority of the forcing is from accelerating the fluid. Even at higher Strouhal number, the fluid acceleration manages to soutweigh viscous effects to attain high efficiency, although the separation becomes noticeable for this oscillating foil behavior. If the acceleration effects are small then the separation forces are significant and the foil passively actuated angular motion and loading will likely be more erratic.

The spring stiffness parameter determines the airfoil's propensity to align with the flow. A higher C inhibits alignment, thus increasing chances of separation and vice versa. Hence, a higher spring constant exacerbates viscous dominated, separated flow and causes a slightly less harmonic pitch profile. However, at high St the foil's downward plung generates large amounts of thrust, so much so that there is only a slight reduction in efficiency due to separation effects mostly occurring during feathering at the top and bottom of the heaving motion.

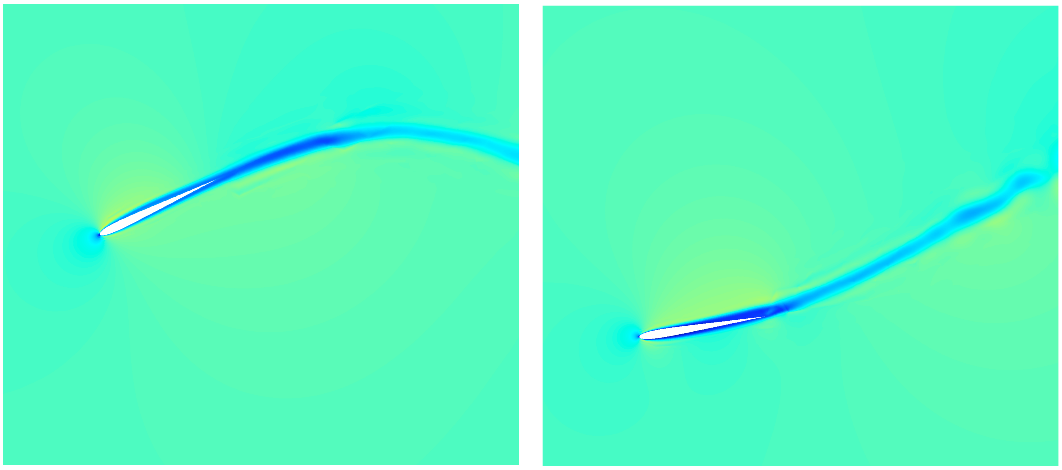

(a) $0.25T$ (b) $0.5T$

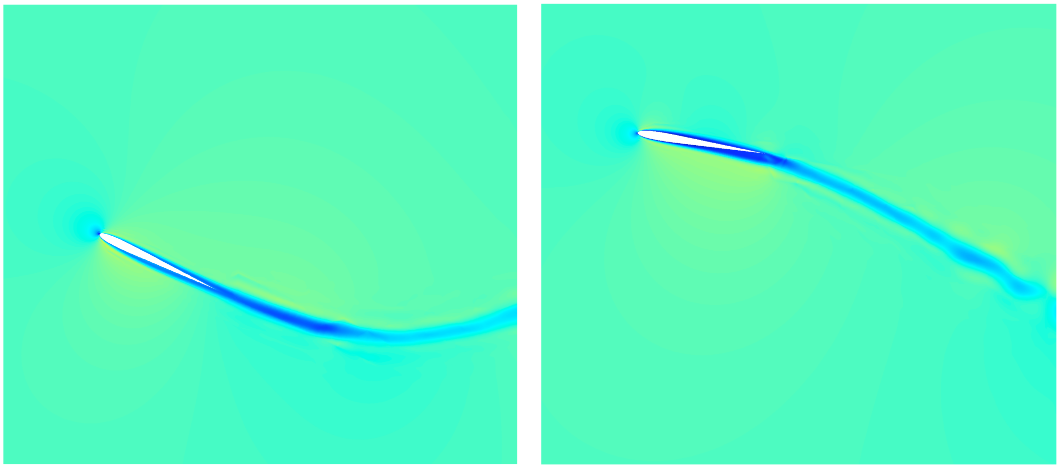

(c) $0.75T$ (d) T

Figure 4-23: Mach contours for the simulation with $k = 0.4$, $St = 0.2$, $C = 0.1$. This flapper is almost completely aligned with the flow clearly depicted by the absence of vortical structures.

Mach contours

The Mach contours for three spring simulations are shown in figures 4-23, 4-24, and 4-25. The Mach colorbar is [0,0.45] where 0 is in blue and 0.45 is in red. The contours visualize the flow phenomena. For stiffer springs and higher St, flow structures, i.e. shedding vortices, appear due to separation as well illustrated in figure 4-25. Otherwise a soft spring and low heaving amplitude simulation involves an airfoil that aligns with the flow minimizing separation effects.

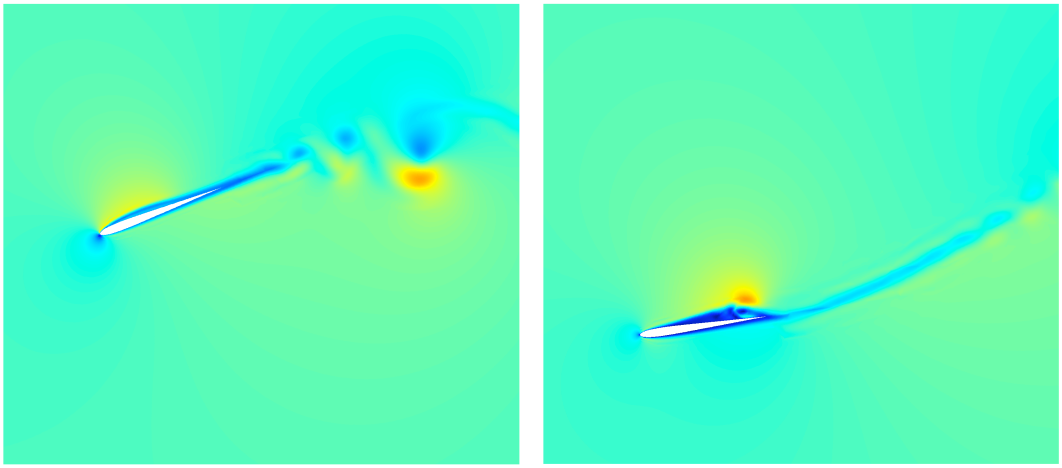

(a) $0.25T$ (b) $0.5T$

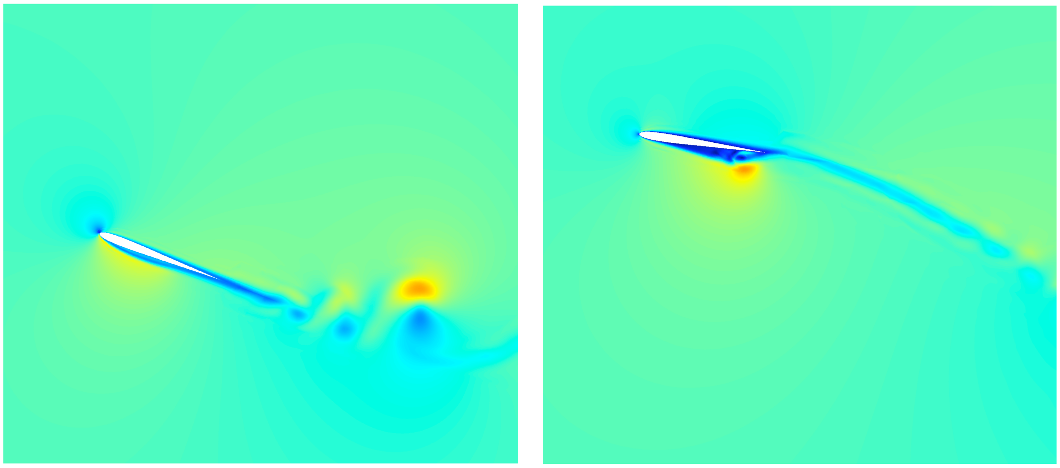

(c) $0.75T$ (d) T

Figure 4-24: Mach contours for the simulation with $k = 0.4$, $St = 0.2$, $C = 0.3$. Setting $St = 0.2$, this oscillating foil has optimal performance compared to other spring stiffnesses.

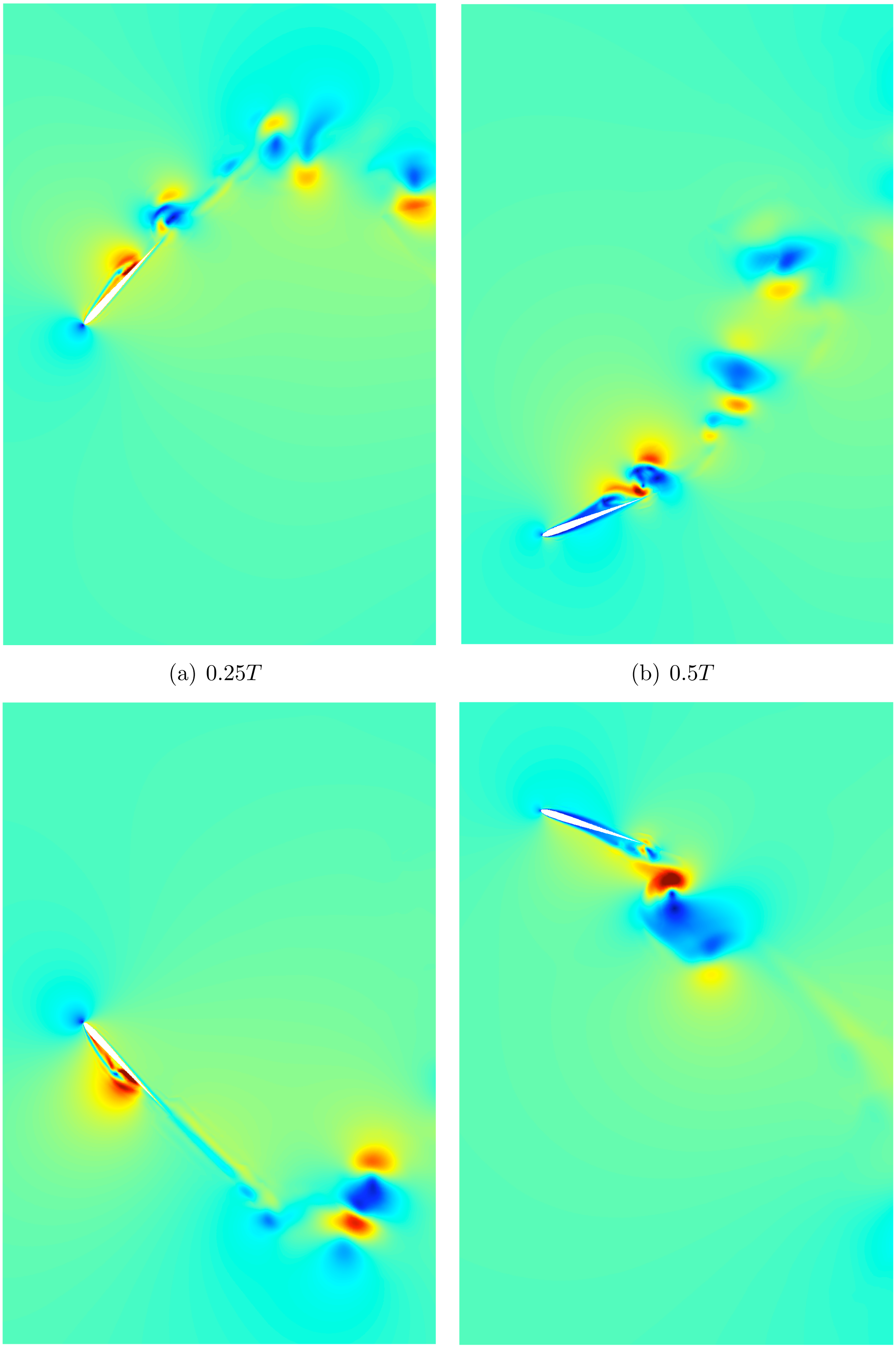
(a) $0.25T$ (b) $0.5T$

(c) $0.75T$ (d) T

Figure 4-25: Mach contours for the simulation with $k = 0.4$, $St = 0.5$, $C = 0.3$. This flapper experiences separation effects, yet is very efficient, $\eta \approx 0.8$.

4.3.3 Prescribed motion vs spring actuation

This section investigates the effectiveness of the spring with respect to prescribing similar kinematics that the passive actuation generates. The four prescribed motion cases involve setting the pitch as θ_{fit} from the Levenberg-Marquardt algorithm and heave using the corresponding St with respect to four spring simulations: $k = 0.4$, $St = 0.1$, $C = 0.1$; $k = 0.4$, $St = 0.3$, $C = 0.4$; $k = 0.4$, $St = 0.1$, $C = 0.5$; $k = 0.4$, $St = 0.5$, $C = 0.5$.

The prescribed motion cases are effective when the spring actuated pitch angle resembles a sinusoid which is in the case of minimal flow separation. The reactiveness of the spring outperforms prescribed sinusoidal motion for stiff spring cases. In this instance, the spring adjusts the pitch angle to alleviate separation effects. For the case $k = 0.4$, $St = 0.5$, $C = 0.5$, the spring enhances the efficiency by 6.8% and the thrust by 27.3% given in table 4.4. It is important to note that the efficiency calculation of the enforced oscillating foil assumes the least power input needed for angular rotation of the foil (see equation (4.6)); thus, the enriched efficiency due to the spring is underestimated. The actuator effectiveness can affect the foil's propulsive efficiency by up to 10% even with the same motion. There is an aerodynamic regime where the spring actuated and prescribed motion perform and behave similarly; however, it is easier if the spring just "automatically" selects the pitch angle as opposed to needing to actuate both heave and pitch. In fact, the prescribed pitch angle is determined from the spring simulations which narrowed the selection of the pitch angle modulation.

Here, the spring is necessary when separation occurs. This result is important

Table 4.4: Prescribed sinusoidal motion results using θ_{fit} compared with actual spring results ($k = 0.4$ for all cases). A negative efficiency is represented by 0.

St, C	θ_{fit} (in °)	η_{spr}	η_{prescr}	$\Delta\eta$	$C_{t,\text{spr}}$	$C_{t,\text{prescr}}$	ΔC_t
0.1, 0.1	$-13.8\sin(0.8t - 18.9)$	0	0	-	-0.0228	-1.221	-
0.3, 0.4	$-32.6\sin(0.8t - 25.9)$	0.6325	0.6369	-7%	0.3317	0.3346	-0.8%
0.1, 0.5	$-9.3\sin(0.8t - 11.3)$	0.2178	0.2247	-3.2%	0.0188	0.0199	-5.9%
0.5, 0.5	$-49.5\sin(0.8t - 7.1)$	0.7119	0.6634	6.8%	0.9630	0.7002	27.3%

with respect to natural flappers. In nature, there are separation effects due to flying at high angles of attack; thus, the spring model is essential in this aerodynamic regime for the pitching and heaving airfoil to be efficient and thrust-producing. Since the spring modulates the airfoil angle when the forces change, it shows the benefit of aero-elasticity in nature.

In terms of engineering design, the spring is an ideal actuator of the foil dynamics. The passive actuation mechanism converts fluid motion into energy without power and is also able to conserve energy within the spring. The pure extraction of energy is a result of the aerodynamic moment inducing the foil's rotational velocity (determining pitch). Furthermore, the spring modulated oscillating foil's energetics is superior to any other actuator.

In conclusion, without the onset of separation the optimized prescribed sinusoids should behave well and comparably to the spring. Despite this region of performance overlap, the spring selects the correct pitch angle naturally, whereas with prescribed kinematics both pitch and heave need to be actively actuated. For separating flow, there is no question the spring can adjust its pitch to alleviate separation which is a feature lacking with prescribed design.

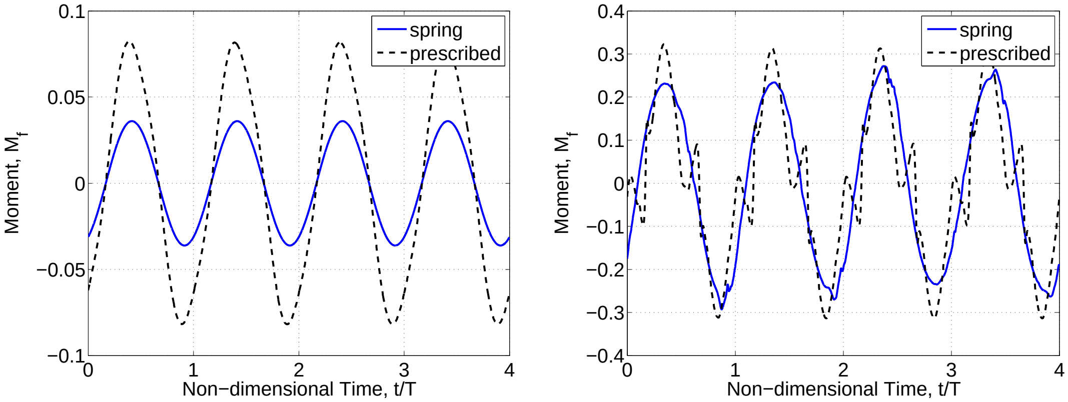

(a) $k = 0.4$, $St = 0.1$, $C = 0.1$ (b) $k = 0.4$, $St = 0.3$, $C = 0.4$

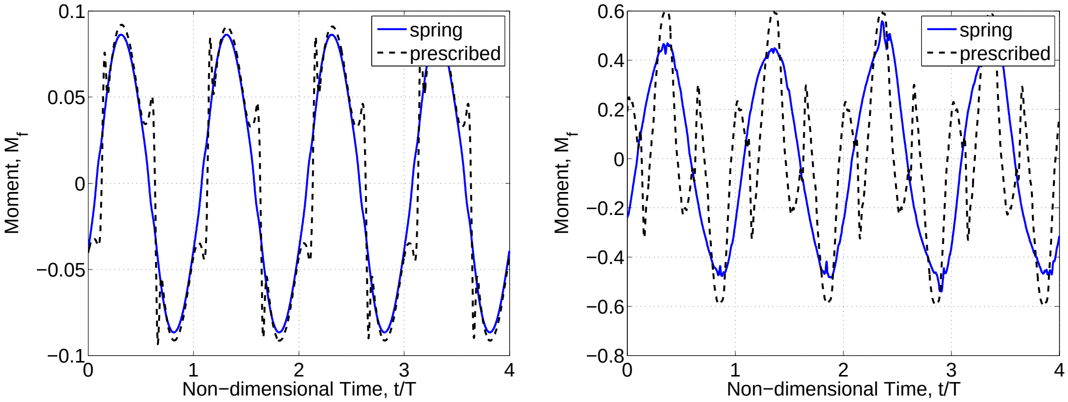

(c) $k = 0.4$, $St = 0.1$, $C = 0.5$ (d) $k = 0.4$, $St = 0.5$, $C = 0.5$

Figure 4-26: A comparison of the time-varying aerodynamic moment or torque between spring actuated flappers and their prescribed analog. For the low amplitude oscillating foil, the passively actuated simulation encounters much smaller moments than the corresponding prescribed harmonic motion.

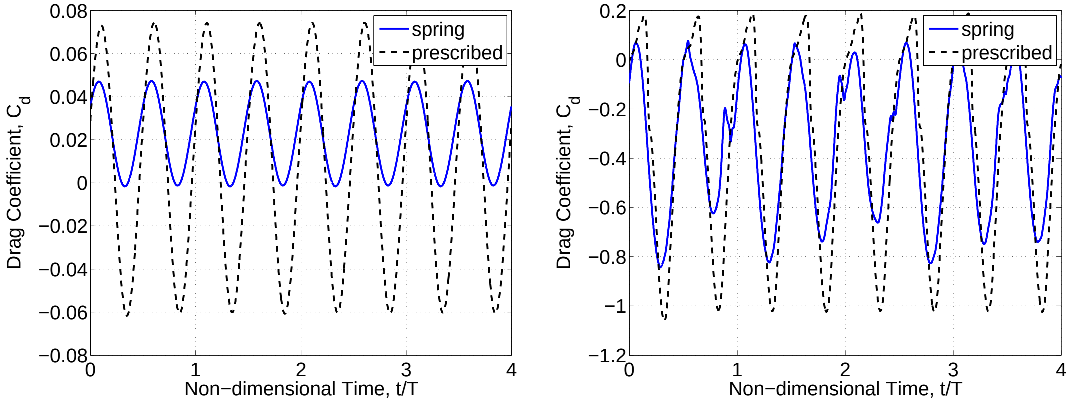

(a) $k = 0.4$, $St = 0.1$, $C = 0.1$

(b) $k = 0.4$, $St = 0.3$, $C = 0.4$

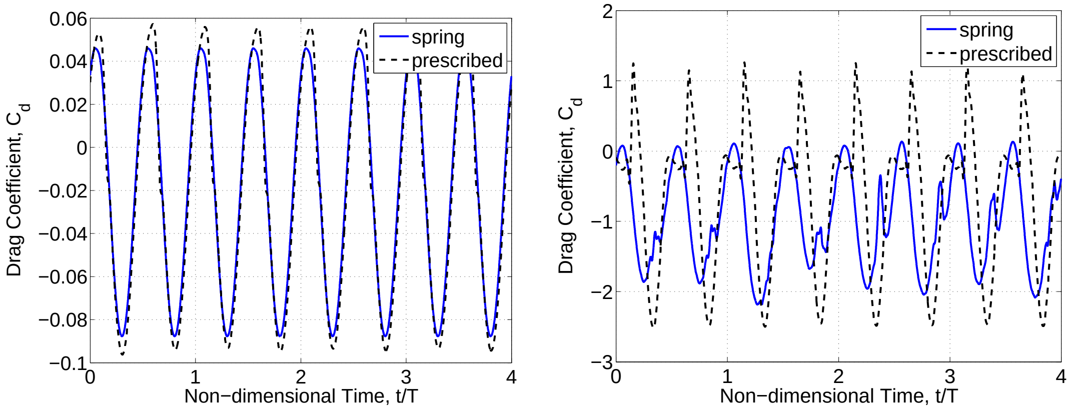

(c) $k = 0.4$, $St = 0.1$, $C = 0.5$

(d) $k = 0.4$, $St = 0.5$, $C = 0.5$

Figure 4-27: The unsteady drag coefficient for both spring actuated and precise harmonic oscillating foils is plotted for four simulations within the high reduced frequency design sweep. Figure 4-27(d) shows the drag results of a highly-separating simulation. It is evident that the passively actuated heaving foil generates more thrust due to the flexibility of its angular motion.

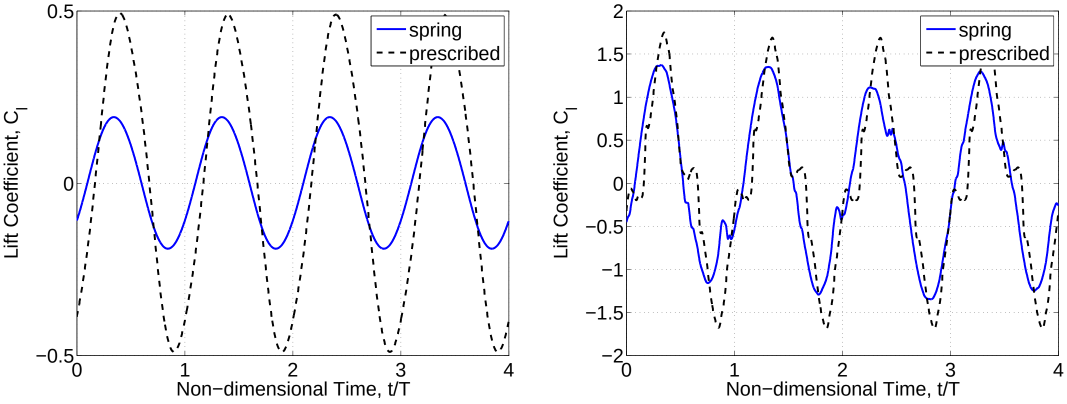

(a) $k = 0.4$, $St = 0.1$, $C = 0.1$ (b) $k = 0.4$, $St = 0.3$, $C = 0.4$

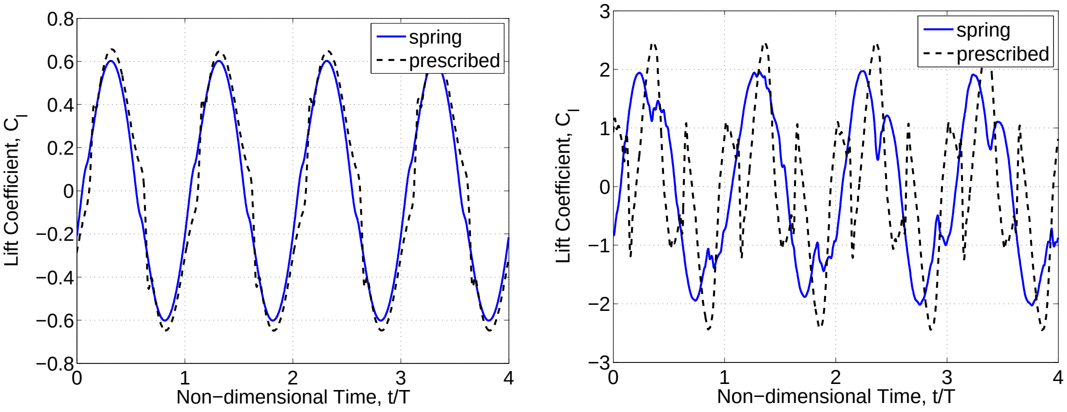

(c) $k = 0.4$, $St = 0.1$, $C = 0.5$ (d) $k = 0.4$, $St = 0.5$, $C = 0.5$

Figure 4-28: A contrast of the spring and its prescribed harmonic analog lift coefficient is indicative of the passive model's smoother force generation even with the onset of separation. This is illustrated in 4-28(b) and 4-28(d).

Chapter 5

Conclusions

5.1 Design sweep trends

In order to conclude, the trends of the design sweep are overviewed in table 5.1 and 5.2. Table 5.1 summarizes the pitch angle profile and instantaneous force generation over the flapping parameter space. The peak of force generation occurs approximately right before the pitch angle maximum or when the airfoil is at zero heave. The table omits magnitudes for simplicity. However, the amplitude of the pitch profile is small for low St cases and large for high St cases with very little dependence on

Table 5.1: Qualitative design space trends for pitch angle, moment and instantaneous forces (drag and lift over time). The amplitude trends of the pitch are summarized in table 4.3. *This occurs more in the low reduced frequency case.

	low C	high C
low St	sinusoidal pitch smooth moment signal smooth force generation	sinusoidal pitch smooth moment signal smooth force generation
medium St	sinusoidal pitch smooth moment signal smooth force generation	triangular-like wave pitch for low k fluctuating moment at peaks* erratic forces at peaks*
high St	slight triangular wave pitch* fluctuating moment at peaks some erratic force generation	asymmetric triangular wave pitch fluctuating moment at peaks some erratic force generation

Table 5.2: Design space trends for efficiency and thrust as well as level of separation.

	low C	high C
low St	not efficient/low efficiency no thrust/very low thrust no separation	low efficiency low thrust, $C_t = [0.05, 0.2]$ no separation
medium St	medium/high efficiency low thrust, $C_t = [0.2, 0.3]$ separation at peak of heaving cycle	medium efficiency medium thrust, $C_t = [0.3, 0.4]$ some separation
high St	medium/high efficiency medium/high thrust, $C_t = [0.4, 0.6]$ separation	highly efficient high thrust, $C_t = [0.5, 0.9]$ severe separation

spring stiffness (see table 4.3). In other words, high amplitude heaving produces high amplitude pitching and vice versa.

Table 5.2 qualitatively summarizes the efficiency and thrust over the design space as well as describes the degree of separation with respect to the flapping parameters, St and C. The presence of separation signifies that the airifoil is experiencing viscous loading. For high amplitude heaving, the loading has a significant viscous force component but still remains acceleration dominated. Thus, the viscous forces remain much smaller than the inertial forces, inducing little reduction in efficiency. Consequently, the high St simulations still manage to be very efficient despite separating effects. On the other hand, in spite of the absence of separation in low St cases, the airfoil does not generate thrust or enough thrust to be efficient and thus is ineffective. The occurrence and severity of separation reflects how well the airfoil aligned with the flow i.e. a low effective angle indicates less chances of separation. A lower spring constant (softer spring) enables the airfoil to better align with the flow by rotating more easily in response to the aerodynamic moment at the top and bottom of the heave cycle. This flow alignment tendency even occurs at high St (see figure 4-15). Moreover, the spring stiffness is a measure of the airfoil's passive structural compliance that naturally modulates the pitch alleviating separation effects.

5.2 Passive compliance

The results of the design sweep simulation suggest that the spring driven airfoil is an advantageous passive flight strategy. The leading edge spring gives the flapping foil structural compliance that also occurs in biological flapping flight. This compliance is lacking in prescribed design. In essence, the spring model has kinematic flexibility whereas the purely prescribed pitching and heaving foil persists with precise periodic motion. In adverse flow conditions, the passive compliance of the spring alleviates separation effects. Moreover, the design sweep illustrates that efficient flapping and thrust production is possible with a pitch modulated airfoil over range of flapping parameters. Thus, the model is capable of generating different levels of thrust.

In summary, the passive leading edge spring compliance represents a strategy to minimize adverse effects of separation and enhance propulsive efficiency. The reactiveness and flexibility of the motion creates a less confined range of flapping parameters than prescribed motions in which flapping still remains effective or well-behaved i.e. efficient, thrust producing flight. Secondly, the prescribed motion needs precise/optimal kinematics to attain high propulsive efficiency which means a design sweep is needed for optimal motion whereas the spring passively drives an efficient, oscillating airfoil. Thus, the spring is similar in principle to the passive compliance exploited in nature. Specifically, the spring models a bat's compliant bones or a bird's feathers as compliant beam members that alleviate adverse environmental conditions when in flight e.g. gusts.

Importantly, the passive spring actuation system is an optimal mechanism to drive the flapping motion. With superior energy extraction and conservation, the spring is an ideal actuator that modulates pitch angle by exploiting the aerodynamic moment. The optimum performance and behavior of the spring dynamical system promotes the utilization of spring actuated oscillating foils in design.

Lastly, the effectiveness of compliance in nature to deal with unpredictable environmental obstacles motivates the investigation of compliant flapping flight. Other active fine-tune adjustments of natural flappers would be modeled with an active control model. Perhaps, a control law could relate the airfoil's pitch to skin friction. By sensing skin friction, the airfoil has another input to determine its dynamics with the objective of minimizing adverse separation effects. A combined active and passive control model is the next step in the attempt to capture the success of natural flappers.

Appendix A

BDF-k nonlinear residuals

Given the BDF-k nonlinear residual defined in equation 2.22, the specific expressions with coefficients are expressed for 1st, 2nd, and 3rd order, respectively

$$\begin{aligned}
R_1 &= M\left(u_n - u_{n-1}\right) + \Delta t R(u_n) \\
R_2 &= M\left(u_n - \frac{4}{3}u_{n-1} + \frac{1}{3}u_{n-2}\right) + \frac{2}{3}\Delta t R(u_n) \\
R_3 &= M\left(u_n - \frac{18}{11}u_{n-1} + \frac{9}{11}u_{n-2} - \frac{2}{11}u_{n-3}\right) + \frac{6}{11}\Delta t R(u_n)
\end{aligned}$$

where the BDF in the subscript is omitted.

Appendix B

Sinusoidal least squares (SLSQ) method

The numeric nonlinear minimization is an iterative method starting with an initial guess $b^{(0)}$ where b is the vector of coefficients or degrees of freedom of the optimization. In this case the fitted parameter vector is the coefficients in equation 4.12 where $b = [\theta_A, \omega, \phi]$. The fitted sinusoid attempts to model the pitch angle profile generated from the simulations. The algorithm minimizes the sum of squares of the deviations

$$S^2(b) = \sum_{i=1}^{N} \left(\theta_i - \theta_{\text{fit}}(t_i; b)\right)^2 . \tag{B.1}$$

The next iterate is linearly approximated by

$$\theta_{\text{fit}}(t_i, b + \epsilon) \simeq \theta_{\text{fit}}(t_i, b) + J_i \epsilon \tag{B.2}$$

where J_i is the gradient of θ_{fit} with respect to b and ϵ is a vector of adjustments to the parameter vector. In sinusoid case in which $b = [\theta_A, \omega, \phi]$, the analytical Jacobian is simply

$$J = \begin{bmatrix} \frac{\partial \theta_{\text{fit}}}{\partial \theta_A} \\ \frac{\partial \theta_{\text{fit}}}{\partial \omega} \\ \frac{\partial \theta_{\text{fit}}}{\partial \phi} \end{bmatrix} = \begin{bmatrix} \sin(\omega t + \phi) \\ \omega \theta_A \sin(\omega t + \phi) \\ \theta_A \sin(\omega t + \phi) \end{bmatrix} \tag{B.3}$$

The minimum of the sum of squares S^2 occurs when the gradient of S with respect to ϵ is 0. By differentiating $S^2(b+\epsilon)$ using the approximation in B.2 and setting the result to zero gives

$$(J'J)\epsilon = J'(\theta - \theta_{\text{fit}}) \,. \tag{B.4}$$

The damped version is

$$(J'J + \lambda I)\epsilon = J'(\theta - \theta_{\text{fit}}) \tag{B.5}$$

where the damping factor λ is adjusted by a factor at each iteration. Marquardt improved the algorithm by scaling each component of the gradient according to the curvature. Consequently, the solution direction moves largely in the direction in which J is small enhancing convergence. The identity matrix I is replaced with the diagonal of the Hessian $J'J$ giving

$$(J'J + \lambda \operatorname{diag}(J'J))\epsilon = J'(\theta - \theta_{\text{fit}}) \,. \tag{B.6}$$

In terms of implementation, the procedure is as follows: given the initial guess $b^{(0)}$, at iteration k

- (*) Compute $\theta_{\text{fit}}^{(k)}$ with $b^{(k)}$
- Compute $S^2(b^{(k)})$
- Set λ
- Solve equation B.6 for ϵ

- Evaluate $S^2(b^{(k)} + \epsilon)$
- If $S^2(b^{(k)}+\epsilon) \geq S^2(b^{(k)})$, increase λ by the factor v ($\lambda = v\lambda$), update the solution $b^{(k+1)} = b^{(k)} + \epsilon$ and go back to (*) for iteration $k+1$
- If $S^2(b^{(k)}+\epsilon) < S^2(b^{(k)})$, decrease λ by a factor v ($\lambda = \lambda/v$), update the solution $b^{(k+1)} = b^{(k)} + \epsilon$ and go back to (*) for iteration $k+1$
- If $\|\epsilon^{(k)}\| <$ tolerance or $S^2(b) - S^2(b+\epsilon) <$ tolerance, stop.

When analyzing the pitch angle profiles, the implementation of SLSQ involved setting the initial guess $b^{(0)} = [\theta_{\max}, 2k, 0]$, the factor $v = 10$, the initial damping factor $\lambda^{(0)} = 0.001$, and the tolerance $= 10^{-6}$.

Bibliography

[1] M. Abdulrahim, K. Boothe, R. Lind, and P. Ifju. Flight characterization of micro air vehicles using morphing for agility and maneuvering. In *SAE World Congress, Reno, NV, SAE-2004-01-3138*, 2004.

[2] H. Ahn and Y. Kallinderis. Strongly coupled flow/structure interactions with a geometrically conservative ale scheme on general hybrid meshes. *Journal of Aircraft*, to appear.

[3] J. M. Anderson, K. Streitlien, D. S. Barrett, and M. S. Triantafyllou. Oscillating foils of high propulsive efficiency. *Journal of Fluid Mechanics*, 360:41–72, 1997.

[4] B. Cockburn and C.-W. Shu. The local discontinuous galerkin method for time-dependent convection-diffusion systems. *SIAM Journal of Numerical Analysis*, 35:2440–2463, 1990.

[5] C. Farhat and P. Geuzaine. Design and analysis of robust ale time-integrators for the solution of unsteady flow problems on moving grids. *Computational Methods Applied Mechanical Engineering*, 193(39-41):4073–4095, 2004.

[6] P. Geuzaine, C. Grandmont, and C. Farhat. Design and analysis of ale schemes with a provable second-order time accuracy for inviscid and viscous flow simulations. *Journal of Computational Physics*, 191(1):206–227, 2003.

[7] K. C. Hall and S. R. Hall. Minimum induced power requirements for flapping flight. *Journal of Fluid Mechanics*, 323:285–315, 1996.

[8] K. C. Hall, S. A. Pigott, and S. R. Hall. Power requirements for large-amplitude flapping. In *35th Aerospace Sciences Meeting and Exhibit, AIAA paper 97-0827*, Jan. 1997.

[9] K. C. Hall, S. A. Pigott, and S. R. Hall. Power requirements for large-amplitude flapping. *Journal of Aircraft*, 35(3):352–361, 1998.

[10] J. S. Hesthaven and T. Warburton. Nodal high-order methods on unstructured grids. i. time-domain solution of maxwell's equations. *Journal of Computational Physics*, 181:186–221, 2002.

[11] C. T. Kelly. *Iterative Methods for Optimization.* SIAM Frontiers in Applied Mathematics, 18 edition, 1999.

[12] K. Levenberg. A method for the solution of certain non-linear problems in least squares. *The Quarterly of Applied Mathematics*, 2:164–168, 1944.

[13] P. B. S. Lissaman. Low-reynolds-number airfoils. *Annual Review Fluid Mechanics*, 15:223–239, 1983.

[14] I. Lomtev, R. M. Kirby, and G. E. Karniadakis. A discontinuous galerkin ale method for compressible viscous flows in moving domains. *Journal of Computational Physics*, 155(1):128–159, 1999.

[15] N.C. Nguyen, P.-O. Persson, and J. Peraire. Rans solutions using high order discontinuous galerkin methods. In *45th AIAA Aerospace Sicences Meeting and Exhibit*, Jan. 2007.

[16] J. Peraire and P.-O. Persson. The compact discontinuous galerkin (CDG) method for elliptic problems. *SIAM Journal of Scientific Computing*, to appear 2007.

[17] P.-O. Persson and J. Peraire. A high order discontinuous galerkin method for fluid-structure interaction. In *18th AIAA Computational Fluid Dynamics Conference, AIAA 2007-4327*, 2007.

[18] P.-O. Persson and J. Peraire. Newton-gmres preconditioning for discontinuous galerkin discretizations of the navier-stokes equations. *SIAM Journal of Scientific Computing*, to appear 2007.

[19] P.-O. Persson, J. Peraire, and J. Bonet. Discontinuous galerkin solution of the navier-stokes equations on deformable domains. In *Proc. of the 45th AIAA Aerospace Sciences Meeting and Exhibit*, January 2007.

[20] W. H. Press, B. P. Flannery, S. A. Teukolsky, and W. T. Vetterling. *Numerical Recipes in C: The Art of Scientific Computing*. Cambridge University Press, Feb 1993.

[21] J. J. Reuther, J. J. Alonso, J. R. R. A. Martins, and S. C. Smith. A coupled aero-structural optimization method for complete aircraft configurations. In *37th AIAA Aerospace Sciences Meeting and Exhibit, Reno, Nevada*, AIAA-99-0187, January 1999.

[22] P. L. Roe. Approximate riemann solvers, parameter vectors, and difference schemes. *Journal of Computational Physics*, 43:357–372, 1981.

[23] J. C. Tannehill, D. A. Anderson, and R. H. Pletcher. *Computational Fluid Mechanics and Heat Transfer*. Taylor & Francis, 1997.

[24] G. K. Taylor, R. L. Nudds, and A. L. R. Thomas. Flying and swimming animals cruise at a strouhal number tuned for high power efficiency. *Nature*, 425:707–711, 2003.

[25] T. Theodorsen. General theory of aerodynamic instability and the mechanism of flutter. Technical Report 496, National Advisory Committee of Aeronautics, 1949.

[26] C. S. Venkatasubban. A new finite element formulation for ale (arbitrary langrangian eulerian) compressible fluid mechanics. *International Journal of Engineering Science*, 33(12):1743–1762, 1995.

[27] D. Viieru, J. Tang, Y. Lian, H. Liu, and W. Shyy. Flapping and flexible wing aerodynamics of low reynolds number flight vehicles. In *44th AIAA Aerospace Sciences Meeting and Exhibit, AIAA-2006-503*, Jan. 9-12, 2006.

[28] Z. J. Wang. Vortex shedding and frequency selection in flapping flight. *Journal of Fluid Mechanics*, 410:323–341, 2000.

[29] D. J. Willis, E. R. Israeli, P.-O. Persson, M. Drela, J. Peraire, S. M. Swartz, and Breuer K. S. A computational framework for fluid structure interaction in biologically inspired flapping flight. In *AIAA Conference, AIAA-2007-4182*, June 2007.

[30] D. J. Willis, J. Peraire, and J. K. White. A combined pfft-multipole tree code, unsteady panel method with vortex particle wakes. *Journal of Numerical Methods in Fluids*, 53:1399–1422, 2007.

[31] D. J. Willis, P.-O. Persson, E. I. Israeli, J. Peraire, S. M. Swartz, and K. S. Breuer. Multifidelity approaches for the computational analysis and design of effective flapping wing vehicles. In *46th American Institute of Aeronautics Aerospace Sciences Meeting and Exhibit, AIAA 2008-518*, Jan. 2008.

[32] Z. Yozibah, R. M. Kirby, K. Meyers, B. Szabò, and G. Karniadakis. High-order finite elements for fluid-structure interaction problems. In *44th AIAA/ASME/ASCE/AHS Structures, Structural Dynamics, and Materials Conference, Norfolk, Virginia*, AIAA-2003-1729, April 2003.